MNRAS 000, 1–19 (2022) Preprint 18 January 2023 Compiled using MNRAS LATEX style file v3.0

On the bright-end of the UV luminosity functions of galaxies at $z \sim 0.6 - 1.2$

M. Sharma[1,2⋆], M. J. Page[1], I. Ferreras[3,4,5], A. A. Breeveld[1]
[1] *Mullard Space Science Laboratory, University College London, Holmbury St Mary, Dorking, Surrey, RH5 6NT, UK*
[2] *Isaac Newton Group of Telescopes, C. Álvarez Abreu, 70, E38700 Santa Cruz de La Palma, La Palma, Spain*
[3] *Instituto de Astrofísica de Canarias, Calle Vía Láctea s/n, E38205, La Laguna, Tenerife, Spain*
[4] *Departamento de Astrofísica, Universidad de La Laguna, E38206, La Laguna, Tenerife, Spain*
[5] *Department of Physics and Astronomy, University College London, Gower Street, London WC1E 6BT, UK*

Accepted XXX; Received YYY; in original form ZZZ

ABSTRACT

We derive the Ultra-Violet (UV) luminosity function (LF) of star forming galaxies falling in the redshift range $z = 0.6 - 1.2$, in the rest-frame far-UV (1500 Å) wavelength. For this work we are in particular interested in the bright end of the UV LF in this redshift range. The data from *XMM-Newton* Optical Monitor (XMM-OM), near-ultraviolet ($1600 - 4000$ Å) observations over 1.5 deg^2 of the COSMOS field are employed for this purpose. We compile a source-list of 879 sources with UVW1$_{AB}$ extending to ~ 21 mag from the wide area UVW1 image of the COSMOS field in the two bins $0.6 \leq z \leq 0.8$ and $0.8 \leq z \leq 1.2$. We use the maximum likelihood to fit a Schechter function model to the un-binned data to estimate the parameters (faint-end slope, characteristic magnitude and normalisation) of the Schechter function. We find that the shape of the LF is consistent with the Schechter model and the parameters are in fair agreement with other studies conducted using direct measurements of the 1500 Å flux. We see a brightening of the characteristic magnitude as we move from lower (0.7) to higher (1.0) redshift. The measures for luminosity density are within the error margins of past studies. We examine the brightest sources in our sample for AGN contribution. These sources are characterised through their spectral energy distributions (SEDs), integrated infrared luminosities and morphologies. We also explore their overlap with the brightest IR galaxies in a similar redshift range.

Key words: galaxies: evolution - ultraviolet: galaxies - ultraviolet: luminosity function - galaxies: luminosity function

1 INTRODUCTION

The luminosity function (LF) is one of the most powerful statistical tools employed to study the distribution of large scale properties (e.g. galaxy masses, luminosities, star formation rates) of a galaxy population under consideration. The galaxies can be arranged based on how much light is coming out of them. Counting these galaxies in a luminosity bin per comoving volume gives a number density traditionally called the luminosity function. In other words, a luminosity function describes the number density of galaxies in a luminosity interval.

The estimation of galaxy LFs is one of the most important problems in extra-galactic astronomy and observational cosmology, for it has multiple applications. An integral of the luminosity function can be used to derive the luminosity density. This luminosity density scales directly with the star-formation rate for UV band measurements (e.g. Lilly et al. 1996; Madau et al. 1998). The LF is widely used to de-project the angular correlation function using Limber's equation (Limber 1953) to estimate the three dimensional spatial distribution of galaxies, and study the large scale properties like the correlation length, halo mass, galaxy bias, and halo occupation (e.g. Hildebrandt et al. 2009a). There are studies proposing to constrain the primordial non-Gaussianities at the small scales (Sabti et al. 2021), and to study the primordial power spectrum (Yoshiura et al. 2020), using the UV LFs at high redshifts. A precise estimate of the faint-end slope is required to estimate the magnification bias in gravitational lensing studies (e.g. Narayan & Wallington 1993), which can be used as an independent probe to study cosmological parameters such as the total matter density, the dark matter power spectrum normalisation and also the

⋆ E-mail: mnushv@gmail.com (MS)

galaxy bias (e.g. Scranton et al. 2005; Hildebrandt et al. 2009b).

The theoretically predicted shape from the $\Lambda-$CDM model comes in the form of the dark matter halo mass function (e.g. Shirasaki et al. 2021). Assuming a baryon fraction and star formation efficiency, the halo mass function can be compared to an observed stellar mass function (Bullock & Boylan-Kolchin 2017). The comparison leads to a mismatch between the two, which becomes severe at the two extremes (high/low stellar masses or bright/faint luminosities; Cole et al. 2001; Yang et al. 2003; Behroozi et al. 2010). Due to this mismatch there is a lot of work going on to understand the nature of physical processes that might be causing the deviations in the observed LF shape with respect to the theoretical predictions. This makes accurate estimates of the LF even more important as these can provide important insights into the additional physical processes occurring at the small scales and help us understand the baryon cycle at those scales (Somerville & Davé 2015). Variation in the shape of the LF as a function of redshift, can be used as a proxy for the evolution of galaxies between different epochs in the history of the Universe.

The stellar evolution in a normal galaxy is believed to dictate many radiative processes occurring in the galaxy, and control the amount of light coming out of it. UV luminosity of galaxies is of particular interest as it is produced mainly by massive stars with short lifetimes (Madau & Dickinson 2014), and can be used to trace the underlying star formation activity in the galaxies over a timescale of 100 Myr. The rest frame 1500 Å emission in the UV is used extensively in the literature as it is one of the most important tracers to understand the star-formation in galaxies. (Kennicutt & Evans 2012).

Using both ground-based and space-borne observatories, many studies have calculated the the UVLF at redshift > 1.2 (e.g. Yoshida et al. 2006; Hathi et al. 2010; Parsa et al. 2016; Moutard et al. 2020). In the redshift range $z < 1.2$ however, there have been only a handful of studies so far because 1500 Å emission can only be accessed from space-borne instruments. The first results on the galaxy UV LF in the redshift range ($0.2 \leq z \leq 1.2$) were obtained by Arnouts et al. (2005) using the NUV data from the *Galaxy Evolution Explorer satellite* (GALEX; Martin et al. 2005). These results were followed up by Oesch et al. (2010) who used data from *Hubble Space Telescope (HST)* WFC3/UVIS instrument to explore the redshift range $0.5 < z < 1$, and by Hagen et al. (2015) who used the UV/Optical Telescope (UVOT) on the *Neil Gehrels Swift* observatory to calculate the LF in the redshift region from 0.2 to 1.2. Using ground-based observations from CFHT and Subaru Telescope, Moutard et al. (2020) and from VLT Cucciati et al. (2012) have calculated the Galaxy LF. Moutard et al. (2020) have re-analysed the GALEX data from Arnouts et al. (2005) to extend their luminosity function to redshifts less than 0.9. Very recently Page et al. (2021) have published their UV LF results in the redshift range of $0.6 < z < 1.2$ using the observations of the 13 Hr field taken through the UVW1 filter of the Optical Monitor telescope onboard the *XMM-Newton* observatory (XMM-OM, Optical Monitor; Mason et al. 2001). In Sharma et al. (2022), hereafter paper I, we have used data from observations of the Chandra Deep Field South (CDFS) taken by the same instrument (i.e. XMM-OM) to estimate the LF from redshift 0.6 to 1.2. This work is a follow up study to paper I and we utilise the UVW1 imaging obtained with the XMM-OM in the wide area Cosmic evolution survey (COSMOS; Scoville et al. 2007) field. With the wide area of this field we expect to find many luminous sources in our survey to extend our LF to brighter absolute magnitudes. We take a look at the properties of the brightest UVW1 sources in COSMOS, and try to establish a connection between the bright UV galaxies and their infra-red (IR) counterparts.

The rest of this paper is structured as follows. All the data and processing (i.e. the observations, UVW1 data, the image processing and the ancillary data used for redshift information and to identify the stars and active galactic nuclei), are explained in section 2. The completeness simulations are also explained in this section. The corrections for Galactic extinction and the K-corrections are discussed in section 3, before final analysis. The methods used to compute the binned LF, fit the Schechter function parameters and the luminosity density are described in section 4. This section also includes the description of the expected effects of cosmic variance. In addition, we give more emphasis to the bright-end of the LF in this section. We fit spectral energy distributions to the sources in the brightest bins of the LF and perform checks on the possibilities for these sources to be AGN. We present our results in section 5, and discuss them in 6. Finally, we conclude this paper in section 7. For this paper we have assumed a flat cosmology with $\Omega_\Lambda = 0.7$, $\Omega_M = 0.3$ and Hubble's constant $H_0 = 70\,\mathrm{km\,s^{-1}\,Mpc^{-1}}$. The distances are calculated in comoving co-ordinates in Mpc. The AB system of magnitudes (Oke & Gunn 1983) is adopted throughout this study.

2 OBSERVATIONS & DATA

2.1 XMM-OM observations of the COSMOS field

The COSMOS field with its wide 2 deg^2 survey area and multi-wavelength coverage from X-ray to radio, has been catering for studies of galaxy evolution and large scale structure over a wide range of redshifts. In this study we use data from XMM-COSMOS (Hasinger et al. 2007; Cappelluti et al. 2007), a wide field survey of the COSMOS field with the XMM-Newton observatory. In particular the data taken by the UVW1 filter of the XMM-OM at a central wavelength of 2910 Å is utilised. The UVW1 data are most relevant to derive the 1500 Å LF at the redshifts $0.6 - 1.2$. For this filter XMM-OM provides a PSF (FWHM) of 2 arcsec. Our catalogue of the XMM COSMOS Survey consists of imaging from 55 observations between December 2003 and May 2007, targeting 25 slightly overlapping pointings spanning the COSMOS field. These 25 pointings are arranged in a 5×5 grid. The final image also contains a 4×4 grid of holes (no data) with typical sizes ranging from 4 to 7.5 arcmin^2 (Fig. 1).

All the imaging is produced in the 'default' (also known as 'rudi-5') configuration, where a setup of 5 consecutive exposures is used to cover 92 per cent of the 17×17 arcmin^2 FOV of the XMM-OM. For details about the image configurations see Mason et al. (2001). More details about the dif-

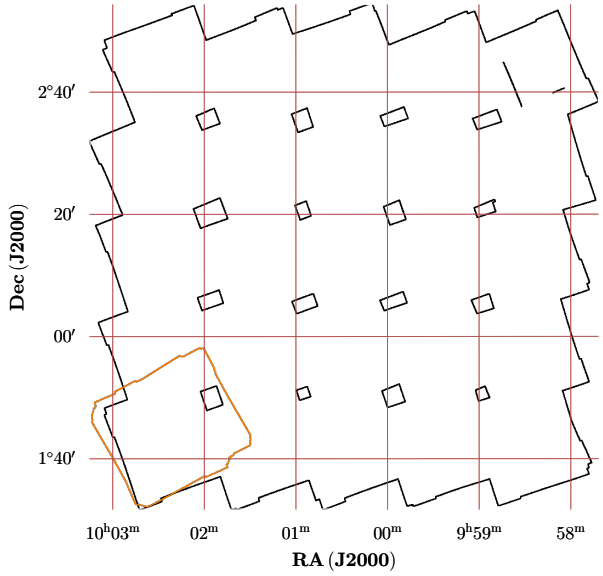

Figure 1. COSMOS vs CDFS : Here we show the footprint of the COSMOS UVW1 image (this work) in black colour and over plot the CDFS (paper I) footprint in the bottom left of the plot in orange. The images are plotted on the same spatial scale to show the contrast in the sky-area of the surveys. The little black squares/rectangles in the COSMOS area indicate gaps between the different pointings, where there is no OM data.

ferent image configurations can also be found in the XMM-Newton User's Handbook[1].

2.2 XMM-OM data reduction and processing

The processing of COSMOS data is done here following the same process as in paper I (i.e. XMM-OM image processsing pipeline with some tweaks). We give a brief summary of the process here, and refer the reader to paper I and Page et al. (2012, 2021) for details. The raw data were obtained from the XMM-Newton Science Archive[2] (XSA). The standard XMM-Newton Science Analysis System[3] task OMICHAIN is used for primary pipeline processing of the data. The data products are removed from the pipeline after correcting for mod-8 pattern for additional processing to get rid of the background scattered light feature at the center of the images, and also to remove some artefacts. The artefacts and their corrections are explained in section 2.2 of paper I. After correcting for all the cosmetic effects, the images were then distortion corrected for any non-linear offsets in pixel positions, aligned with the equatorial coordinate frame of SDSS DR12 (Alam et al. 2015) then rotated and re-binned into sky coordinates using the SAS task OMATT. Finally, the images were co-added using the SAS task OMMOSAIC. The spatial extent of the final co-added COSMOS image can be seen in Fig. 1 as compared to the smaller but deeper CDFS image used in the paper I.

The final image is then fed to the SAS task OMDETECT,

[1] https://xmm-tools.cosmos.esa.int/external/xmm_user_support/documentation/uhb/omdef.html
[2] https://www.cosmos.esa.int/web/xmm-newton/xsa/
[3] https://www.cosmos.esa.int/web/xmm-newton/sas

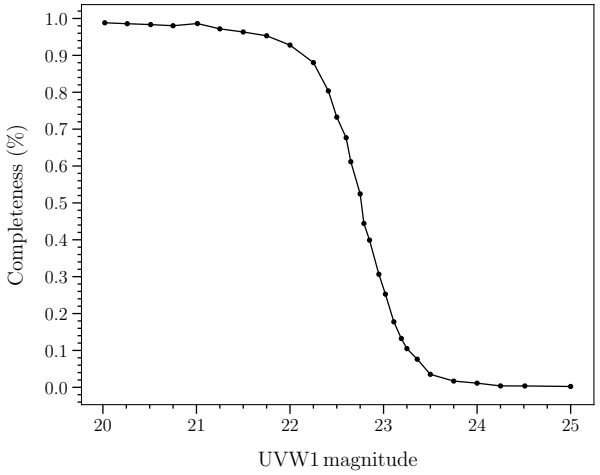

Figure 2. Completeness of the source detection as a function of UVW1 magnitude, as determined from the simulations described in Section 3.1. The black data points represents fraction of recovered simulated galaxies at each input UVW1 mag. Confusion limit is represented by the red coloured shaded area at the bottom of the plot.

which performs the photometry and source detection, using different algorithms for identifying point and extended sources. For point-like sources, the default photometric aperture used by OMDETECT depends on signal to noise ratio, with brighter sources measured in a 5.7 arcsec radius aperture, and fainter sources measured in a 2.8 arcsec aperture (Page et al. 2012). Most of the UVW1-detected galaxies with redshifts between 0.6 and 1.2 appear point-like to XMM-OM, and the brightest of these would by default be measured in a 6 arcsec aperture. Inspection of deep optical images of these luminous galaxies reveals that photometry in such a large aperture will be contaminated by the light from other surrounding galaxies. Therefore we have forced omdetect to adopt the smaller 3 arcsecond radius aperture for bright, as well as faint galaxies, within our sample. In total 7027 sources are detected in the UVW1 image above a signal to noise threshold of 4.

The edges of the images are areas of low signal to noise, resulting in spurious sources entering the catalogue. To get rid of this problem we mask the outer 10 pixels of the COSMOS UVW1 image. Due to this masking we lost 0.046 deg^2 (2.9 per cent) of sky area and 102 (1.4 per cent) of the sources.

2.3 Completeness

The completeness of a survey is affected by various factors, primarily signal to noise ratio, but also the blending of two or more faint sources into one i.e. source confusion. In order to quantify how complete (or incomplete) as a function of magnitude our galaxy sample is, we use the same technique as in paper I. We briefly discuss the process here and refer the reader to paper I and Page et al. (2021) for details.

We simulate artificial point sources of varying magnitudes, add them to the real image and detect them using OMDETECT (section 2.2). If a source is detected within a circular region of radius 1 arcsec of the position of the in-

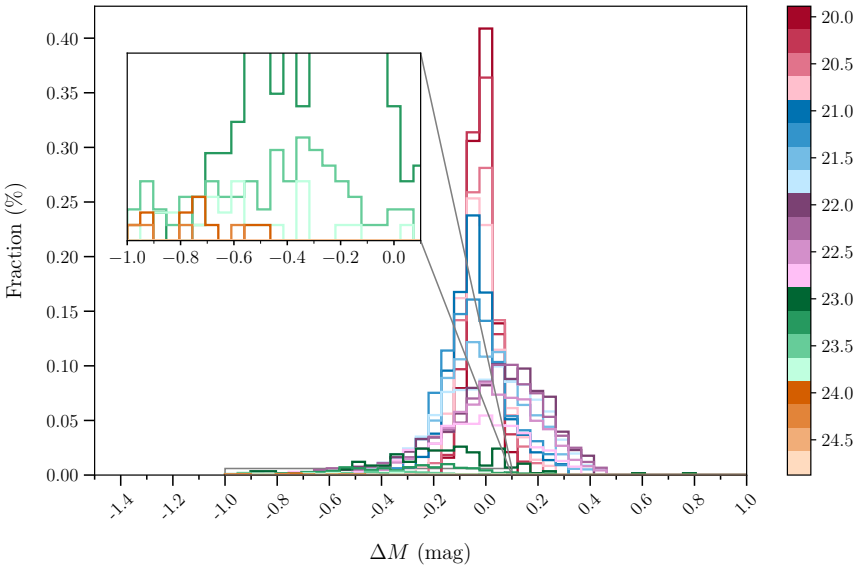

Figure 3. The distributions of the magnitude errors in the detection process at each simulated UVW1 magnitude, where x-axis show the magnitude offsets between the inserted and recovered sources and the y-axis represents the fraction of sources at each offset. Each colour, as represented by the discrete colourbar represents the input magnitude in the completeness simulations. The inset window represents a part the plot stretched in the y-axis for clarity.

serted source, we consider the source as recovered. At least 1000 sources are used at each input magnitude ranging from UVW1 mag 20 to 25 in steps of 0.25 mag, with smaller step sizes of 0.05, 0.10 and 0.15 between magnitudes 22.25 to 23.50, where completeness drops quickly. Before we calculate the quantities required for our further analysis, the simulations are corrected for the reddening and the edge-mask (section 2.2) applied on our final image.

The recovery fraction at a particular magnitude defines the completeness. This fraction is plotted as a function of UVW1 AB magnitude in Fig. 2 and is used in section 4.1 to calculate the binned LF. The distributions of the magnitude offsets between the inserted and recovered sources are used as the error distributions, as they contain information of the unknown systematics unique to the XMM-OM, the UVW1 filter and the detection process. These distributions are plotted as a function of simulated UVW1 magnitudes in Fig. 3. Each colour represents a simulated UVW1 magnitude ranging from UVW1 mag 20 to 24.75. These distributions are forward folded with the LF models in order to obtain the observed distributions, before the maximum likelihood fitting is performed (section 4.2) to obtain the LF parameters.

As it can be seen in Fig. 2, our catalogue is found to be $>$ 98 per cent complete for UVW1 $<$ 21 mag, 75 per cent complete at UVW1 $\leq$ 22.5 mag and falls $<$ 10 per cent as UVW1 magnitude goes beyond 23.25. At UVW1 24 mag the recovery fraction goes down to $<$ 1 per cent. From Fig. 3 (see inset), it can be seen that the magnitude offset distribution is lying at the negative values mostly for UVW1 mag 23.75 and completely for UVW1 mag $>$ 24, implying that the recovered sources are brighter than the ones inserted.

This means that sources fainter than UVW1 mag 24 are only detected due to flux boosting - faint sources blended with the noise spikes. We notice that the faintest output magnitude of a detected source is 24.25, which is also apparent from the completeness plot, where above 24.25 magnitudes the completeness curve becomes more or less of an asymptote to the magnitude axis. We conclude that at around this magnitude (UVW1 24.25 mag), we hit the sensitivity limit for the survey (i.e. at fainter magnitudes than this, we can not get any detections) and we are not limited by confusion. In order to be on the safe side, we take the conservative approach similar to paper I and apply a magnitude limit brighter than the faint detection limit. We choose UVW1 23.11 mag (= 23.02 mag after reddening correction) as the magnitude limit for our survey. The completeness level at this magnitude is 47 times the residual level at the sensitivity limit.

2.4 Ancillary data

Once we have our source-list, with UVW1 magnitudes, we combine it with other catalogues from the literature to collect additional information about our sources. We use this additional information to identify the stars and AGNs in our sample, and to assign redshifts to our galaxies. Similar to paper I, we perform a test to find out the appropriate search radius to cross correlate our source-list with other catalogues. As we are matching a large catalogue of UVW1 sources to a very deep multi-wavelength catalogue with a much higher sky density, a naive positional match has the potential to generate a large number of spurious matches. Therefore we have explored carefully the matching criteria.

There should be a limit to how blue the UVW1$-u$ colours of star-forming galaxies can be. So, a UVW1$-u$ colour cut can be used with a large matching radius to achieve a high matching rate while keeping the spurious matches to a minimum. We find this blue limit in Appendix A, by comparing the UVW1 and u colours of stars, QSOs and galaxies. We also check what fraction of total

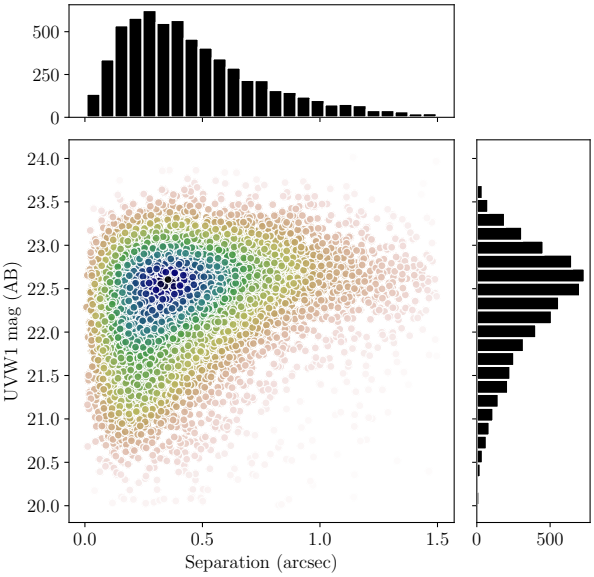

Figure 4. A joint distribution of the UVW1 AB magnitudes of the sources and the angular offsets with their respective counterparts after matching them with Laigle et al. (2016) catalogue using 1.5 arcsec as the maximum offset radius. The histograms represent the marginal distributions.

sources are spuriously matched, in catalogues compiled using different matching radii. From Fig. A2 and A3, we obtain a value -0.5. Since we do not consider reddening effects, we put a conservative limit UVW1$-u > -1$ on our sources and find a matching radius of 1.5 arcsec.

2.4.1 Stars

We have used several different sources to identify the stars in our source-list. The first one is the catalogue from Leauthaud et al. (2007) who use two alternate methods to differentiate the stars from other sources. We also use spectroscopic identifications of stars from Prescott et al. (2006); Trump et al. (2009); SDSS - III (Alam et al. 2015) and Hasinger et al. (2018).

In addition, we employ GAIA DR2 (Gaia Collaboration et al. 2018) data and remove sources with significant proper motions. We define the significant proper motions to be those for which the values are at least more than three times the standard errors. We also use Marchesi et al. (2016) who use both spectroscopic identification and photometric SEDs to identify stars. In total we identified 1523 stars in our catalogue, which constitute $\sim$ 23 per cent of sources in our edge-masked COSMOS UVW1 source-list. For the rest of the analysis, we remove these stars from our source-list.

2.4.2 Redshifts

We merge the remainder of our sources with catalogues containing spectroscopic and photometric redshifts. Following are the brief details of the catalogues.

We use redshifts from the hCOSMOS (Damjanov et al. 2018), which surveyed the COSMOS field with the MMT Hectospec multi-fiber spectrograph. We prioritise their data from the central $\sim$ 1 deg^2 of the field, which (hCOS20.6) is 90 per cent complete to the limiting r magnitude 20.6. We used a set of spectroscopic redshifts compiled by Alarcon et al. (2021) released as part of their PAUS photometric catalogue. Then we add data from the zCOSMOS-bright survey (Lilly et al. 2007; Knobel et al. 2012), which provides high-quality spectroscopic redshifts up to redshift 1.2 for sources with $I_{\rm AB} \leq 22.5$. Next we use the catalogue from Hasinger et al. (2018), who used the Deep Imaging Multi-Object Spectrograph (DEIMOS) on the Keck II telescope. We further add spectroscopic redshifts from the following : Fiber Multi-Object Spectrograph (FMOS) - COSMOS survey (Kashino et al. 2019) which uses medium resolution spectroscopy to obtain $>$ 5000 redshifts, the PRism MUlti-object Survey (PRIMUS; Coil et al. 2011) targeting faint galaxies with the Inamori Magellan Areal Camera and Spectrograph (IMACS) spectrograph on the Magellan I Baade 6.5 m telescope and the Large Early Galaxy Census (LEGA-C; van der Wel et al. 2016) Survey of K-band selected galaxies using the VIMOS spectrograph mounted on ESO's Very Large Telescope. The last few spectroscopic redshifts are from Paulino-Afonso, Ana et al. (2020), who used VIMOS, Prescott et al. (2006) and Trump et al. (2009) who used Hectospec multiobject spectrograph and IMACS respectively on the MMT 6.5 m telescope.

For photometric redshifts we primarily use the the photometric part of the PAUS (Alarcon et al. 2021) catalogue and the $K_{\rm s}$ selected photometric catalogue from (Muzzin et al. 2013) which contains photometry from $0.15 - 24\mu$m. Then we add the Galaxy And Mass Assembly 10h region (G10; Davies et al. 2015), which contains the best photometric redshifts from PRIMUS and Ilbert et al. (2009). We also use photometric redshifts from the following works : the near-infrared selected photometric catalogue created using imaging from various telescopes covering more than 30 photometric bands (COSMOS2015; Laigle et al. 2016); the CANDELS-COSMOS survey (Nayyeri et al. 2017), which is conducted with 42 photometric bands ranging from 0.3 to 8 μm; a volume limited and mass complete sample of COSMOS2015 (Darvish et al. 2017) and the updated edition of the Chandra COSMOS-Legacy (C-COSMOS) Survey Marchesi et al. (2016). In addition to above mentioned catalogues, we utilise data from the SDSS-III DR12 (Alam et al. 2015) to obtain the photometric redshifts for our UVW1 sources.

We tabulate all these catalogues in Table 1 with the number of redshifts taken from each catalogue and the quality flags used to constrain each catalogue to the best possible (most secure) redshifts. In total we get 4578 redshifts out of which 3658 ($\sim$ 80 per cent) are spectroscopic. The distribution of the UVW1 magnitudes of the sources and their distances from counter-parts in COSMOS2015 catalogue are plotted in Fig. 4.

2.4.3 AGNs

The UV contribution from the central super-massive black holes in active galaxies may dominate the emission coming from the star forming regions, in a UV survey. It is the latter emission that we are concerned with in this study. So, the inclusion of UV-bright AGN in the sample can induce an overestimation in the UV LF calculations. In particular, they

Table 1. Need to change now! Catalogues used for spectroscopic and photometric redshifts, along with the number of redshifts and quality flags (QF) used for each catalogue. $z68$ represents the 68 per cent confidence interval around each photometric redshift in the photometric catalogues.

Source Catalogue	Number[a]	QF
Spectroscopic		
Damjanov et al. (2018)	1805	e_Z < 0.0002
Alarcon et al. (2021)	983	2
Knobel et al. (2012)	317	mult[a]
Hasinger et al. (2018)	67	$2, \geq 1.5$[b]
Kashino et al. (2019)	13	> 1
Coil et al. (2011)	459	1[c]
van der Wel et al. (2016)	11	mult[d]
Paulino-Afonso, Ana et al. (2020)	1	none
Trump et al. (2009)	1	q_z > 2
Prescott et al. (2006)	1	none
Photometric		
Alarcon et al. (2021)	559	none
Davies et al. (2015)	35	≤ 2
Muzzin et al. (2013)	198	1
Laigle et al. (2016)	2	z68< 0.1
Alam et al. (2015)	122	e_zph< 0.1[e]
Darvish et al. (2017)	1	0
Marchesi et al. (2016)	3	none

[a] Multiple constraints : cc = x.5, where x = 3, 4, 9, 13, 14, 18 on the first selection and then, cc = y.2−y.4, where y = 3, 4, 9, 13, 14, 18, 23, 24, 29 and cc = z.5, where x = 2, 12, 22.
[b] We use the second quality Flag for the second run.
[c] We choose this quality flag for the first run, and then on the second run we remove this condition and use secondary targets as well.
[d] f_z= 0 and f_spec= 0 and f_use= 1.
[e] e_zph< 0.1 and q_mode= + and mode= 1 and Class= 3.

affect the bright end of the UV LF. We use the same method as in paper I, i.e. to use a X-ray luminosity cut to handle the quasar contamination. The X-ray catalogues from Marchesi et al. (2016); Trump et al. (2009) and Prescott et al. (2006) are used to identify any X-ray sources in the sample. Any sources cross-correlated with Marchesi et al. (2016) and having a luminosity greater than 10^{42} ergs sec^{-1} in the $0.5-10$ KeV, $0.5-2$ KeV or $2-10$ KeV X-ray bands, were removed. In addition to this, sources identified as quasars by Prescott et al. (2006) or identified as having broad-line features by Trump et al. (2009) were also removed. The above criteria identify 97 sources in the UVW1 source-list as quasars. We remove all these sources from further analysis. It is important to remark about the possibility of some AGN making their way into the final catalogue, despite the luminosity cut described here, because the X-ray observations are not sufficiently deep to detect all AGNs with X-ray luminosities $> 10^{42}$ erg s^{-1} in our redshift range. We perform more tests to characterise these bright UV sources in section 4.5.

After this step, we have 4481 sources in our source-list. The UVW1 magnitude distribution of this source-list is plotted in Fig. 5. Finally, a sub-sample of 879 galaxies has been selected with redshifts of the highest quality within a range $0.6-1.2$, 637 of which are spectroscopic. The final redshift distribution of this sub-sample is shown in Fig. 6.

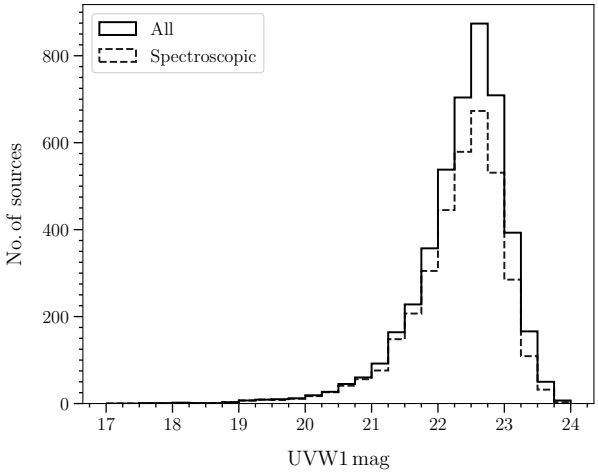

Figure 5. The distribution of the COSMOS UVW1 sources as a function of their UVW1 magnitudes. The solid histogram shows all sources with redshifts and the dashed histogram represents the sources with spectroscopic redshifts.

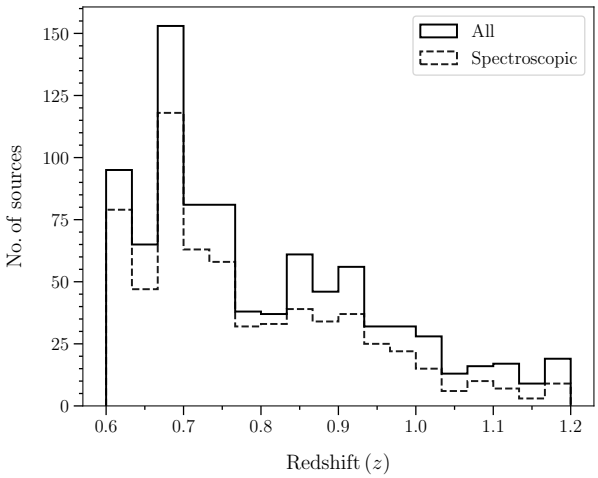

Figure 6. Redshift distribution of the COSMOS UVW1 sample. The spectroscopic redshifts are represented by the dashed line and the sum of spectroscopic and photometric redshifts is represented by the solid line.

3 CORRECTIONS

Before the UVW1 magnitudes are converted into 1500 Å absolute magnitudes and used for calculating the LFs, we need to calculate two important corrections, that we will apply to the absolute magnitudes.

3.1 Galactic extinction

All extra-galactic surveys, especially in the blue part of the galaxy spectral energy distributions (SEDs) are affected by extinction from Galactic foreground dust. We calculated the extinction correction for COSMOS source-list in a similar way to paper I and Page et al. (2021). We use an extinction calibration together with a dust map to calculate the Galactic extinction of the UVW1 sources in the direction of the COSMOS field using Schlegel et al. (1998) and Schlafly &

Table 2. The first five rows of the UVW1 source catalogue used in this work. The columns list the positions, redshifts (z) and the apparent UVW1 magnitudes. The full table is available in the machine readable form with the online version of the paper.

RA (J2000) deg	DEC (J2000) deg	z	UVW1 mag
150.423	2.583	0.82	21.06
149.889	2.735	0.71	21.07
150.666	2.025	0.80	21.26
149.815	2.830	0.85	21.45
150.758	2.238	0.60	22.46

Finkbeiner (2011). For this study we find a value 0.09 magnitudes for Galactic extinction in UVW1. This corrections is added to the calculation of absolute magnitude for each source. The sample is made available as a supplementary table with the online version of the paper. The first five rows of the table are shown in Table 2.

3.2 K-correction

The observed SED of a galaxy appears different from the rest-frame SED as it gets red-shifted due to the expansion of the Universe. So, depending upon the redshift of a source a single waveband may be looking at totally different parts of the galaxy SEDs. This will affect the calculation of absolute magnitude of a source in that given waveband and cause erroneous results. To avoid this effect we have to add a compensating term to the absolute magnitudes of the galaxies in our sample. This compensating term is called the K-correction (Hogg et al. 2002), which is defined as a ratio of fluxes in the rest-frame and the observed (red-shifted) band. Page et al. (2021) describes the methodology used to calculate the K-correction for each UVW1 source. The calculated corrections for each source are plotted in Fig. 7. As in paper I, the K-corrections $K\,(z)$ are added to the expression calculating the 1500 Å absolute magnitudes from the apparent UVW1 magnitudes,

$$M_{1500}\,(z) = m - 5\log\left(\frac{d_L\,(z)}{\mathrm{Mpc}}\right) - 25 - K\,(z) - X_{\mathrm{UVW1}}, \quad (1)$$

where X_{UVW1} is the extinction correction from section 3.1 and $d_L\,(z)$ is the luminosity distance.

4 LUMINOSITY FUNCTION AND LUMINOSITY DENSITY

Once all the corrections are applied to the sample, we divide the sample in two redshift bins covering $0.6 < z < 0.8$ and $0.8 < z < 1.2$. After this we calculate the binned LF, estimate the Schechter function parameters and in the end we determine the UV luminosity density. This section outlines the formalism for all these calculations. We also outline the method we employ to construct the spectral energy distribution (SEDs) for the brighest sources.

4.1 Binned luminosity function estimate

In the volume-magnitude space, we define the binned luminosity function as the number of galaxies N_{bin} inside the bin bound by redshift interval $z_{\mathrm{min}} < z < z_{\mathrm{max}}$ and magnitude interval $M_{\mathrm{min}} < M < M_{\mathrm{max}}$, divided by the effective survey volume enclosed by that bin (Page & Carrera 2000),

$$\phi\,(M, z) \equiv \phi = \frac{N_{\mathrm{bin}}}{V_{\mathrm{bin}}}. \quad (2)$$

The effective survey volume inside each bin V_{bin} is a 4-volume in the volume-magnitude space given by,

$$V_{\mathrm{bin}} = \int_{M_{\mathrm{min}}}^{M_{\mathrm{max}}} \int_{z_{\mathrm{min}}}^{z_{\mathrm{max}}} \frac{\mathrm{d}V\,(z)}{\mathrm{d}z}\,\mathrm{d}z\,\mathrm{d}M, \quad (3)$$

where z_{min} and z_{max}, the lower and upper extremes of the redshift interval are calculated as

$$z_{\mathrm{min},\,i} = \min\left(z_{\mathrm{min}},\, z\,(M_i,\, m_l)\right), \quad (4)$$

and

$$z_{\mathrm{max},\,i} = \max\left(z_{\mathrm{max}},\, z\,(M_i,\, m_u)\right), \quad (5)$$

where m_l and m_u are the lower and upper magnitude limits of the survey, $z\,(M_i,\, m_l)$ and $z\,(M_i,\, m_u)$ are the minimum and maximum redshifts at which the object i can be found and still be within the magnitude limits of the survey. The term $\mathrm{d}V\,(z)\,/\mathrm{d}z$ in the integrand of equation 3 is obtained as a product of effective area and the differential comoving volume element,

$$\frac{\mathrm{d}V\,(z)}{\mathrm{d}z} = \left(\frac{\pi}{180}\right)^2 \int_{\Omega} \mathcal{A}_{\mathrm{eff}}\,(M)\,\frac{\mathrm{d}V\,(z)}{\mathrm{d}z\,\mathrm{d}\Omega}\,\mathrm{d}\Omega \quad (6)$$

where $\mathcal{A}_{\mathrm{eff}} = \mathcal{A} \cdot C\,(m)$ is the effective area, obtained by multiplying the sky-area ($\mathcal{A}$) by the completeness function $C\,(m)$. We tabulate the effective areas along with the completeness as a function of the UVW1 magnitudes in Table 3.

$$\frac{\mathrm{d}V\,(z)}{\mathrm{d}z\,\mathrm{d}\Omega} = \frac{c\,H_0^{-1}\,d_L^2}{(1+z)^2\,[\Omega_\lambda + \Omega_m(1+z)^3]^{1/2}} \quad (7)$$

is the differential comoving volume element (Hogg 1999).

From Poisson's statistics (Gehrels 1986), we calculate the uncertainty for N objects and hence the statistical uncertainty in the LF for each bin. The resulting luminosity function ϕ has units of $\mathrm{Mpc}^{-3}\mathrm{mag}^{-1}$.

Table 3. The COSMOS UVW1 survey has different levels of completeness at different magnitudes, hence the effective sky area changes with UVW1 magnitude. Using the completeness simulations we associate each limiting magnitude with a completeness fraction (second column). The effective area ($\mathcal{A}_{\mathrm{eff}}$) is the product of the completeness fraction and the geometric sky area of the survey and is given in the third column.

UVW1 magnitude (AB mag)	Completeness (per cent)	Effective Area (deg^2)
19.93	98.83	1.5088
21.66	95.30	1.4550
22.16	88.04	1.3441
22.32	80.36	1.2269
22.41	73.24	1.1182
22.56	61.17	0.9339
22.66	52.44	0.8007
22.76	39.90	0.6094
22.86	30.65	0.4679
22.93	25.26	0.3855
23.02	17.76	0.2711

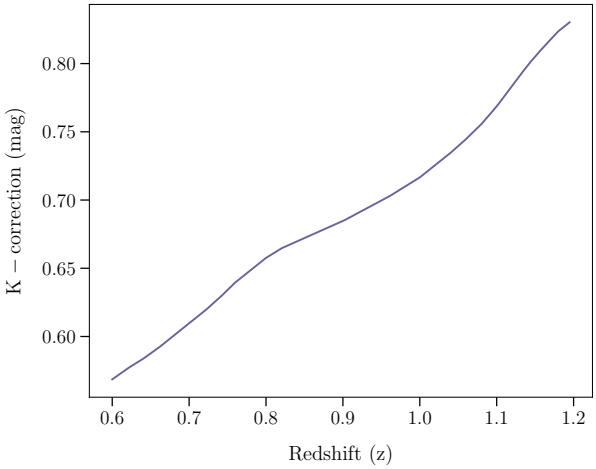

Figure 7. K-corrections made to the absolute magnitude of each source in our UVW1 source-list as a function of their redshifts.

4.2 Schechter function parameters

We analyse the galaxy distribution in the redshift - magnitude space by comparing it to a galaxy LF model using maximum likelihood. We use the Schechter function (Schechter 1976) to model the galaxy LF in each redshift bin. It is parametrised as,

$$\phi(M) = 0.4 \ln 10 \, \phi^* \times 10^{-0.4(M-M^*)(1+\alpha)} \exp\left(-10^{-0.4(M-M^*)}\right) \quad (8)$$

the product of an exponential function and a power law, which dictate the shape at bright and faint magnitudes respectively. The shape transitions from the power law of slope α, to the exponential form at the knee of the LF, described by M^*. The LF is normalised by the characteristic number density ϕ^*.

We convolve the Schechter function model with the error distributions (see Fig. 3) obtained from the completeness simulations in section 2.3. These histograms are normalised by the number of sources for each magnitude that are inserted into the image.

Given the LF parameters $\theta = (\phi^*, M^*, \alpha)$, the probability distribution such that a galaxy of magnitude M_i is observed at a redshift z_i, can be expressed as,

$$p\left(M_i', z_i \,|\, \theta\right) \propto \frac{p\left(\theta \,|\, M_i', z_i\right)}{p\left(\theta\right)}, \quad (9)$$

and the likelihood function for N_G galaxies can be written as,

$$\mathcal{L} = \prod_i^{N_G} p\left(M_i', z_i \,|\, \theta\right). \quad (10)$$

This likelihood function can be written in a more convenient form as

$$S = -2 \ln \mathcal{L} = -2 \sum_{i=1}^{N_G} \ln p\left(M_i', z_i\right), \quad (11)$$

and it can be minimised in order to maximise $\mathcal{L}$.

We obtain the posterior probability distributions for the Schechter function parameters (ϕ^*, M^*, α) using the Markov Chain Monte Carlo (MCMC) method, assuming a uniform uninformative prior $p\left(\theta\right)$. To implement MCMC, we use PYTHON module EMCEE (Foreman-Mackey et al. 2013).

Table 4. Derived Schechter function parameters of the galaxy UV LF from their respective posterior distributions at both redshift bins. Errors indicate 1σ (68.26 per cent) uncertainties.

z	$\phi^*/10^{-3}$ (Mpc^{-3})	M^*	α
$0.6 - 0.8$	$5.05^{+0.75}_{-1.07}$	$-19.12^{+0.20}_{-0.22}$	$-1.37^{+0.48}_{-0.43}$
$0.8 - 1.2$	$1.76^{+0.43}_{-0.64}$	$-19.83^{+0.26}_{-0.29}$	$-1.66^{+0.59}_{-0.55}$

Table 5. Cosmic variance errors on normalisation calculated using two alternate methods explained in section 4.4. We tabulate the average stellar masses (second column) in both redshift bins (column 1). The last column shows 1σ fractional errors in normalisation calculated using Trenti & Stiavelli (2008) (I) and Moster et al. (2010) (II).

z	$M_*/10^{10}$ ($M_\odot$)	$\Delta\phi^*/\phi^*(1\sigma)$	
		I	II
0.7	1.43	0.103	0.111
1.0	1.73	0.083	0.069

4.3 UV Luminosity density

Once the Schechter function parameters are determined for our survey, the luminosity density can be derived by integrating the product of luminosity with the luminosity function,

$$j = \int_0^\infty L \, \phi\left(L\right) \, \mathrm{d}L, \quad (12)$$

using equation 8 with $L/L^* = \exp[-0.4 \ln 10 \cdot (M - M^*)]$, we can write

$$j = \int_0^\infty L \, \phi^* \left(L/L^*\right)^\alpha \exp\left(-L/L^*\right) \mathrm{d}\left(L/L^*\right). \quad (13)$$

This gives us a more robust quantity than normalisation (ϕ^*) of the LF to compare our results with past works and avoids the degeneracy in ϕ^* and M^*. We integrate from $M_{1500} = -10\,(L_{1500} = 4.3 \times 10^{24}\,)$ to $M_{1500} = -24\,(L_{1500} = 1.7 \times 10^{30}\,)$ to get the luminosity density. The errors on the normalisation due to cosmic variance (section 4.4) are included in addition to the statistical errors in our calculation of the luminosity density.

4.4 Cosmic Variance

The LF estimates are prone to errors due to the large-scale matter distribution in the Universe. Due to the variation in the matter density, the number counts of the galaxies fluctuate from one part of the universe to another. This effect is most severe for surveys with small sky areas (Somerville et al. 2004; Moster et al. 2010). In this section we calculate the effects of this so-called cosmic variance on our estimates. We use two independent methods, proposed by Trenti & Stiavelli (2008) and Moster et al. (2010) to obtain cosmic variance induced errors on the characteristic number density (or the normalisation) ϕ^* of the Schechter function form of the LF. The first one introduced by Trenti & Stiavelli (2008),

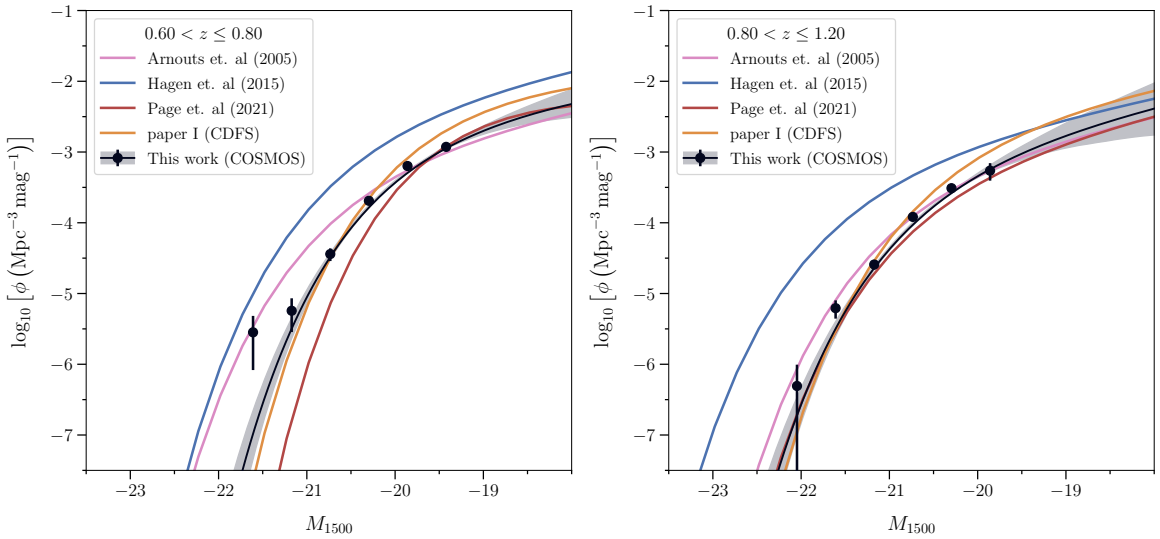

Figure 8. UV luminosity function of galaxies in the redshift intervals $0.6 \leq z < 0.8$ in the left panel and $0.8 \leq z < 1.2$ in the right panel as a function of the 1500 Å magnitude. The data points show the binned number densities measured using the Page & Carrera (2000) method. The black solid line is our best-fitting Schechter function derived from the CDFS field as described in Section 4.2. We obtain this curve from the median value of the posterior distribution of Schechter function parameters. The grey shaded area around the best-fit Schechter function represents the 1σ (68.26 per cent) uncertainties. The blue and red and purple solid lines are the Schechter functions obtained by Arnouts et al. (2005), Hagen et al. (2015) and Page et al. (2021).

calculates cosmic variance using an approach in which the N-body simulations are used to produce mock surveys which in turn are used to calculate the average bias of the sample. The other method suggested by Moster et al. (2010), estimates the cosmic variance using the N-body simulated mocks from the sky-area of the survey, the mean and size of the redshift bin, and the stellar masses of the galaxies probed.

In the web tool provided by Trenti & Stiavelli (2008), we assume values for σ_8 and an average halo occupation fraction of 0.8 and 0.5 respectively along with the bias formalism of Sheth & Tormen (1999). It gives us 1σ fractional errors of 0.103 and 0.083 on normalisation.

As mentioned earlier, the method from Moster et al. (2010) needs the stellar masses. So, we match our final UVW1 source-list to COSMOS/UltraVISTA K_s-selected catalogue (Muzzin et al. 2013) with a matching radius 1.5 arcsec to get the stellar masses of our galaxies. The matching provides 495 stellar masses (96.5 per cent of our sources), which average to 1.51×10^{10} M$_\odot$ in the redshift bin $0.6-0.8$. For these solar masses we get a relative 1σ error of 0.111 from the Moster et al. (2010) code. Following the same procedure for the redshift bin $0.8 - 1.2$, we get 349 (95.4 per cent) counterparts with stellar masses for our sources, giving an average stellar mass 1.87×10^{10} M$_\odot$ and a relative 1σ error on normalisation of 0.069, due to cosmic variance.

The cosmic variance errors on the parameters, calculated using tools from both Trenti & Stiavelli (2008) and Moster et al. (2010) are tabulated in Table 5. The error bars on the normalisation due to cosmic variance are 67 and 43 per cent smaller than 1 σ statistical uncertainties. We expect this result because of the large area the COSMOS field covers.

4.5 Spectral energy distributions

We fit spectral energy distributions (SEDs) to the galaxies in the brightest magnitude bins in both redshift ranges to examine their nature. We obtain the rest frame photometry for our sources in different filters from UV to mid-IR, by matching the positions to the COSMOS 2015 (Laigle et al. 2016) catalogue. For sources that do not have photometry in Far-IR bands, we use the deblended catalogue from Jin et al. (2018) and the HerMES catalogue (Herschel Multi-tiered Extragalactic Survey; Oliver et al. 2012).

An SED model comprising two components is fitted to the photometry. The first component is the stellar emissions from the galaxies and the other component is from the dust emissions coming from the star forming regions. The stellar emission templates are created using stellar population synthesis models of Bruzual & Charlot (2003), assuming a Chabrier (2003) initial mass function for solar metallicity. The sources we have at hand are very bright UV galaxies, so we need stellar emission models for a very young population of stars. We chose models of single stellar population (SSP) with a varying age from 0.01 to 13.18 Gyr, in 30 steps of size log age $\sim$ 0.1. These templates are reddened by assuming the Calzetti et al. (2000) dust extinction model, with the $E(B-V)$ values ranging from 0.0 to 4.0 in steps of 0.14. In total we have 900 stellar emission models. We complement these with the the mid to far infra-red models created by Draine & Li (2007). The cold dust component of our SED constitutes a linear combination of models with constant and variable radiation fields, along with varying amounts of the PAH fraction. Since we are dealing here with bright/large galaxies, so the SMC and LMC models from Draine & Li (2007) are not included in our library. From the SED fits, we calculate their total far infrared luminosities by integrating the total dust model from 8 to 1000 μm. The bolometric lu-

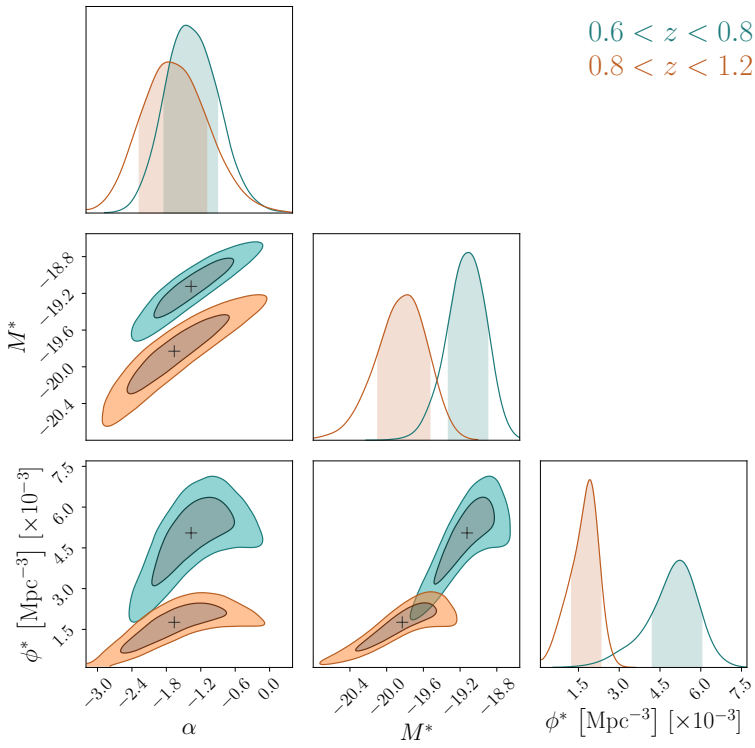

Figure 9. This figure represents the marginalized one dimensional (along the diagonal) and two dimensional (off-diagonal) posterior distributions of Schechter function parameters α, M^* and and ϕ^*. The redshift bin $0.6 \leq z < 0.8$ is represented by blue and redshift bin $0.8 \leq z < 1.2$ is shown in red colour. The shaded region in the dark and light coloured areas in the off-diagonal part of the plot correspond respectively to 68 and 95 per cent confidence intervals for LF parameters. The black '+' symbols represent the median values for α, M^* and ϕ^*. The shaded region in the diagonal plots represent the one dimensional 68 per cent confidence region.

minosity is obtained by integrating the total SED fit within $0.01 - 1000\mu$m.

5 RESULTS

The galaxy rest-frame UV LF in the redshift range $0.6 < z < 1.2$ is derived using the method developed by Page & Carrera (2000), explained in section 4.2. We produce our results by dividing the sample in two redshift bins $0.6 < z < 0.8$ and $0.8 < z < 1.2$. The results for both the bins are plotted in Fig. 8, along with the best-fit Schechter function models from Arnouts et al. (2005); Hagen et al. (2015); Page et al. (2021) and paper I at the same redshifts.

We show in Fig. 9, the one and two dimensional posterior distributions for the LF parameters, obtained by MCMC simulations. The dark and light shaded regions show the 68 and 95 per cent confidence regions for the Schechter function parameters. The best-fit values obtained using the maximum likelihood method presented in section 4.2 are listed in Table 4.

In Fig. 10, we show the comparison of results obtained by this study and from paper I, for redshift bins centered at $z = 0.7$ and $z = 1.0$ respectively. The top panels compare the binned and model LF whereas the bottom panels compare the parameter space, for both redshift bins.

We compare our Schechter function parameters to estimates obtained by past works in the same redshift range in Fig. 12.

Our estimates for the luminosity density are plotted with values from the literature in Fig. 13, and tabulated in Table 6.

6 DISCUSSION

We calculate the UV LF of galaxies using UVW1 data from the wide area COSMOS field. This work complements paper I, in which LFs were calculated from deep UVW1 imaging in the CDFS, in that the larger sky area of COSMOS provides access to a larger sample of the most luminous galaxies, and so we can construct LFs to brighter absolute magnitudes. We can see in Fig. 10 (upper panels), that the wide area COSMOS survey extends the bright end of the LF by almost a magnitude in the redshift bin $0.6-0.8$ and half a magnitude at $0.8 - 1.2$ compared to the CDFS LFs. As a consequence of this we can probe space densities an order of magnitude lower in COSMOS than CDFS, of order 10^{-6} Mpc^{-3} Mag^{-1}.

Our measurements are fairly consistent with the Schechter function shape at both redshift bins. We can see this in the top right panel of Fig. 10, where the observed binned LF follows the shape of the modelled Schechter function. A similar behaviour is observed in the redshift bin $0.6-0.8$ (top left of Fig. 10), except at the brightest absolute magnitude bin, in which the binned LF appears to exceed considerably the Schechter function model. We therefore examine this bin in more detail to determine whether the data

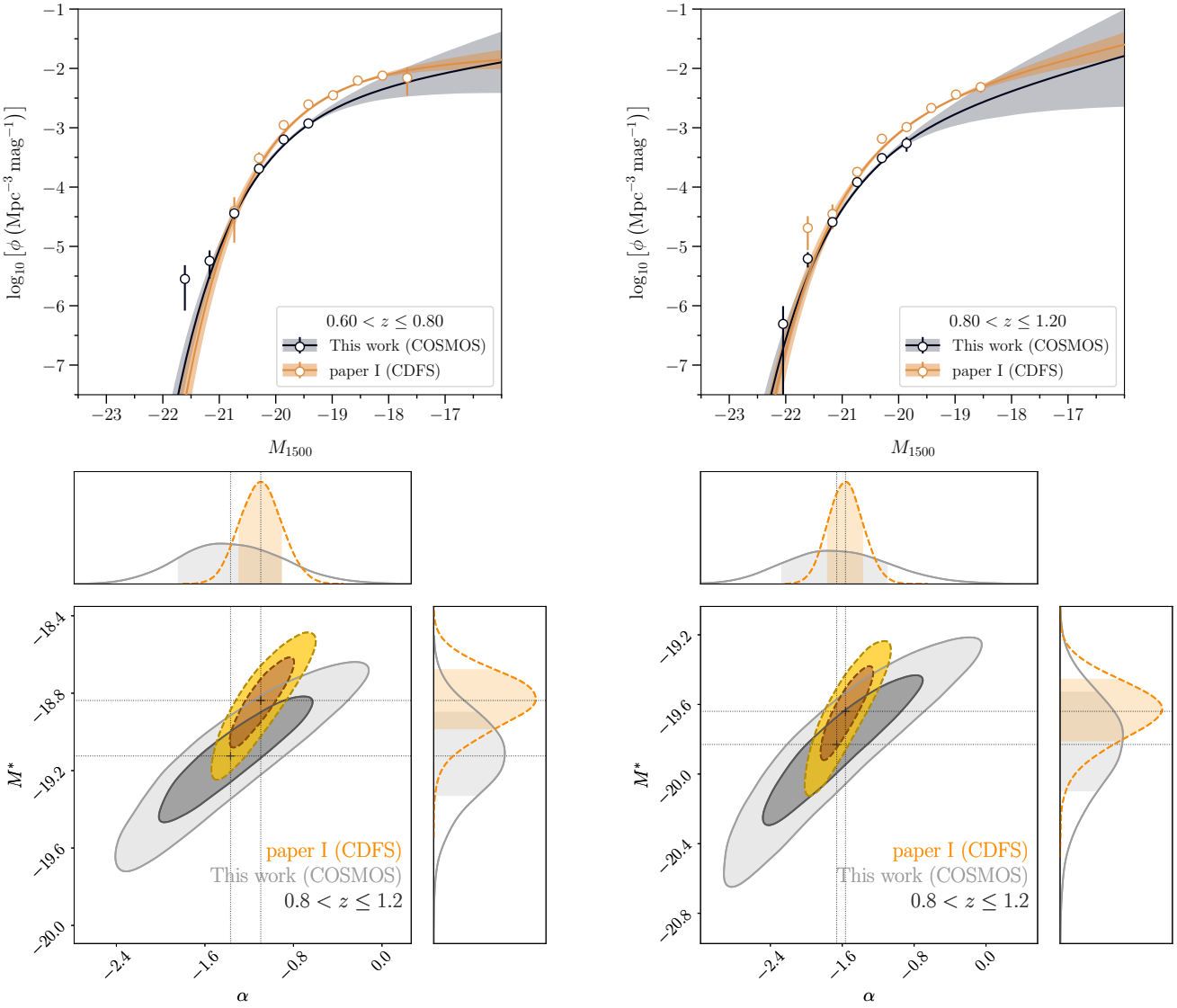

Figure 10. The comparison of the UV galaxies luminosity function of the CDFS (yellow) and COSMOS (black/gray) in the redshift interval $0.6 - 0.8$ (left) and $0.8 - 1.2$ (right). Upper left and right panels : The data points show the binned number densities and the solid lines are maximum likelihood fitted Schechter functions. The shaded regions represent the 1σ uncertainties respectively for redshift bins $0.6 - 0.8$ and $0.8 - 1.2$. Lower left and right panels : The one and two dimensional marginalised distributions in the $M^* - \alpha$ space for the COSMOS (gray) and CDFS (yellow), for lower and higher redshift bins. The dark and light shaded regions represent the 1σ and 2σ confidence regions, and the '+' symbols denotes the median value of the parameters.

in this bin pose a serious challenge to the Schechter function model.

In this brightest absolute magnitude bin, we calculate from the Schechter function model that the expected number of sources in our survey is 0.12, whereas the number of galaxies observed is 2. From Poisson statistics, the probability of observing two or more galaxies when the expected number is 0.12 is 7.1×10^{-3}, a discrepancy that is a little less than 3σ, but still somewhat uncomfortable.

Given this observed discrepancy, we have looked in more detail at the sources in the brightest absolute magnitude bins in both magnitude ranges, and in particular at the possibility that they are contaminated by AGN.

Some potential AGN candidates might be missed by the X-ray detection because the X-ray observations do not reach 10^{42} ergs s^{-1}cm^{-2} in all three bands ($0.5 - 10$, $0.5 - 2$ and $2 - 10$ KeV) out to redshift 1.2 (refer to section 2.4.3). Therefore it is possible that there are AGN which are hiding below the X-ray detection limit and are present in our final UVW1 source-list. In the construction of the LF, there is a significant potential for AGN contamination at the high luminosities where the number densities are very low. So, caution must be taken especially at the bright-end of the LF.

The first step we take to address this issue is to examine the mid-IR properties of these brightest sources. There are two sources in the brightest absolute magnitude bin in the $0.6 - 0.8$ redshift range and a single source in the brightest absolute magnitude bin between redshifts 0.8 and 1.2. For these sources, we obtained the magnitudes in the W1

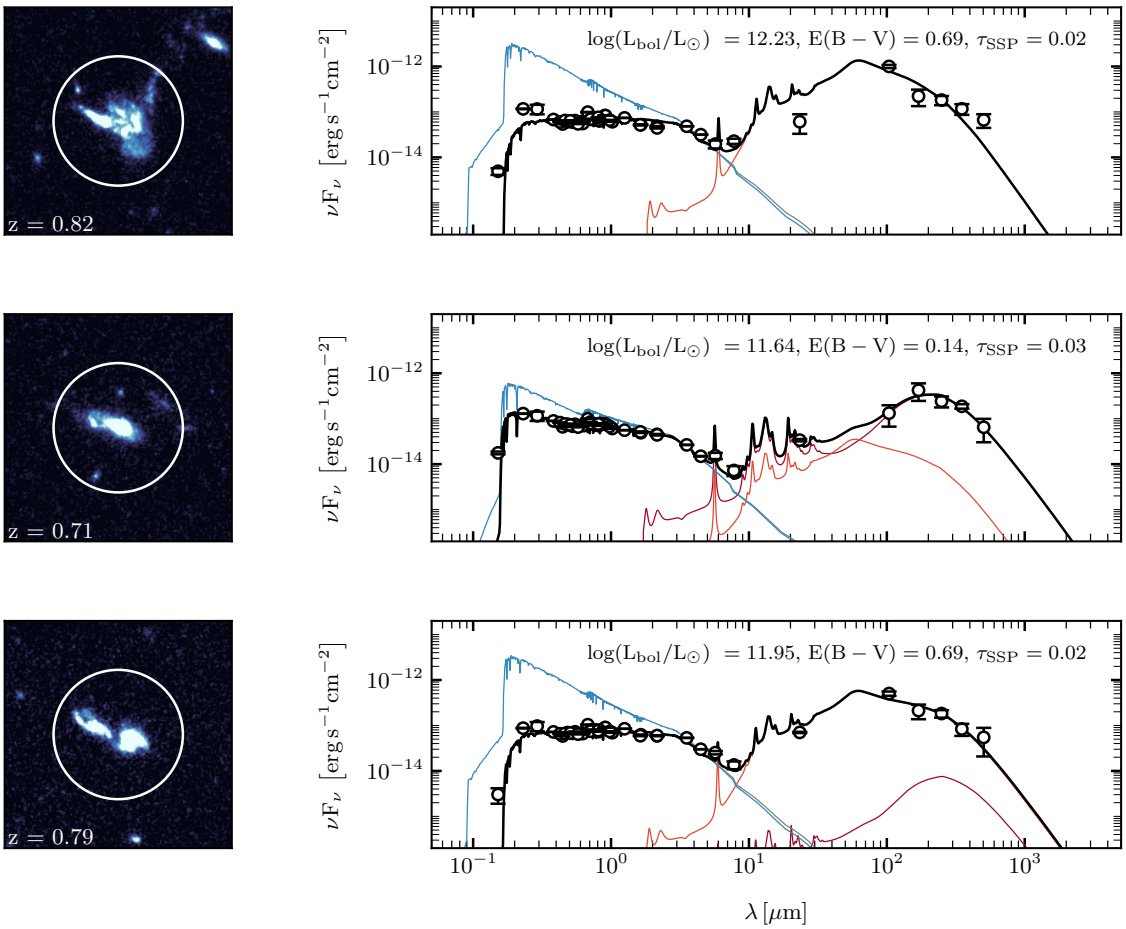

Figure 11. We plot here the SEDs and *HST* ACS stamps of the brightest star forming galaxies in our sample. The *top* row shows the most luminous (UVW1 AB 21.15 mag) source in the redshift bin $0.8-1.2$; the *middle* and the *bottom* rows show two (UVW1 AB mag = 21.16, 21.35) of the most luminous objects in the redshift range $0.6-0.8$. These sources constitute the brightest magnitude bin of their respective redshift bins. The panels on the left show the *HST* ACS stamps of these sources and their redshifts and the right hand side panels show the SEDs. The size of the stamps is 10×10 sq arcseconds. A circular aperture (3 arcsec radius) used for UVW1 photometry COSMOS image is also shown in white colour. The panels on the right hand side show the SEDs. The total SEDs, shown in black solid lines, represent the linear sum of the stellar models generated using Bruzual & Charlot (2003) and the two infra-red models from Draine & Li (2007), one for a constant (orange) and another for a variable (maroon) radiation field. The blue line represents the stellar model with no reddening (i.e. $E(B-V)=0$). In each SED panel we also show the, the fitted age of the simple stellar population (in Gyr), the colour excess and the bolometric luminosity.

(3.4μm) and W2 (4.6μm) passbands of the *Wide-field Infrared Survey Explorer* (*WISE*; Wright et al. 2010) and the 3.6 and 4.5 μm passbands of the *Spitzer* Infrared Array Camera (IRAC; Fazio et al. 2004). We checked the sources against the mid-IR identification criterion set out for *WISE* colors by Stern et al. (2012) and Assef et al. (2013). Similarly, for IRAC colours we used the prescription from İkiz et al. (2020). None of these sources satisfy the conditions outlined for the *WISE* and IRAC colours, by the above mentioned works. So, none of the sources populating the highest luminosity bins in our LFs show evidence for a substantial energetic contribution from an AGN.

To look further at these three sources we examine their SEDs. We also examined their morphology using the COSMOS image from the *Hubble Space Telescope* (*HST*) Advanced Camera for Surveys (ACS) which employed the F814W filter (Koekemoer et al. 2007). The SEDs along with the 10×10 arcsecond postage stamp images are shown in Fig. 11.

As seen in Fig. 11 these luminous galaxies are detected from the far-UV to the sub-mm wavelengths. We fit SEDs containing stellar and dust components (section 4.5). The fits suggest that all three objects have young stellar populations and significant amounts of dust. We obtain their total IR luminosity by integrating the dust components. These sources cover a range in IR luminosities from $4.39\times10^{11}\,L_\odot$ to $1.69\times10^{12}\,L_\odot$. So, these most powerful UV-selected galaxies in the COSMOS field correspond to (U)LIRGs. These systems are defined by their total infrared luminosity as – LIRGs; $10^{11}L_\odot < L_{\rm IR}(8-1000\mu{\rm m}) < 10^{12}L_\odot$ and ULIRGs; $10^{12}L_\odot < L_{\rm IR}(8-1000\mu{\rm m}) < 10^{13}L_\odot$ (Sanders & Mirabel 1996; Genzel et al. 1998). However none of these systems are as luminous as the most powerful IR galaxies in the redshift range under consideration. Kartal-

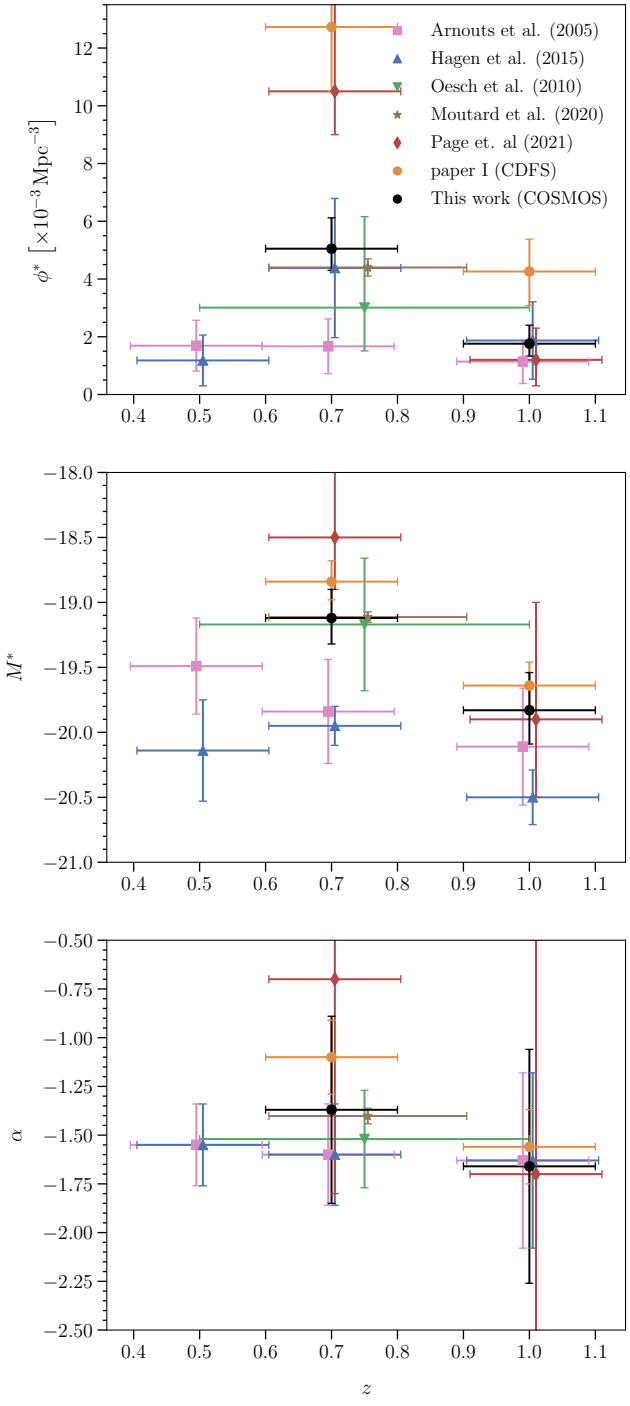

Figure 12. The parameters α and M^* and $\phi*$ of the Schechter function as defined in equation 8 and tabulated in Table 4. The values estimated from this paper are in black. Other colours are used for values estimated by other studies of Arnouts et al. (2005); Hagen et al. (2015); Oesch et al. (2010); Moutard et al. (2020); Page et al. (2021) and paper I. Different panels from top to bottom represent the normalisation $\phi*$, characteristic magnitude M^* and faint-end slope α as function of redshift. The horizontal and vertical error bars represent the width of the redshift bin and 1 σ (68.26 per cent) uncertainties respectively. For clarity the values of parameters at same redshifts are slightly shifted in redshift.

tepe et al. (2010) in their 70 μm selected catalogue find sources as bright as $\sim 8 \times 10^{12}\,\mathrm{L}_\odot$ in a redshift range similar to ours. One of the reasons we do not find any such sources could be that the most powerful IR galaxies are bright AGNs (Sanders & Mirabel 1996; Kartaltepe et al. 2010; Goto et al. 2011; Symeonidis & Page 2021), which we remove from our analysis. The other reason could be the UV selection, as the brightest IR galaxies could be too obscured to be seen strongly at the UV wavelengths.

The examination of the HST images suggests that the morphology of at least two of these three sources constitute mergers in various stages. One of the sources in the 0.6-0.8 redshift bin appears to be an early stage merger with two discrete luminous galaxies within the XMM-OM UVW1 photometry aperture. The identification of this UVW1 source as two discrete galaxies offers a solution to the discrepancy between the observed and model-predicted number of galaxies in the brightest absolute magnitude bin at $0.6 < z < 0.8$. If the UV emission of the galaxies were measured separately, their individual UV absolute magnitudes may well place them in a different bin of the luminosity function. Thus the number of observed galaxies in this most-luminous bin may only be one, rather than two, in which case the discrepancy is no longer significant, and we no longer observe a deviation from the Schechter-function shape at the bright end.

We move on to compare our LFs to those found in previous studies and begin by seeing how our results compare to paper I. In terms of M^* and α the bottom of Fig. 10 shows that the contours from our study and those from paper I overlap. The best-fit values of the faint-end slope and the characteristic magnitude are within 1σ and 2σ of each other respectively for redshift bin centered at $z = 0.7$ and 1σ each for $z = 1.0$. The contours for the CDFS are smaller, which shows that the LF parameters are better constrained as compared to the COSMOS field. We attribute this to the depth of the CDFS UVW1 survey, which probes fainter absolute magnitudes and hence covers the transition between exponential and power law parts of the Schechter function as well as the faint end slope.

Overall our values of the UV LF parameters are in accordance with findings reported by Arnouts et al. (2005). The faint-end slope estimates of $\alpha = -1.60 \pm 0.26$ and -1.63 ± 0.45 from their study are within 1σ from our estimate of $\alpha = -1.37^{+0.48}_{-0.43}$ and $-1.66^{+0.59}_{-0.55}$, for redshift bins at $z = 0.7$ and $z = 1.0$ respectively. We do see a slight deviation in their LF however, in the redshift range $0.6 < z < 0.8$ (left panel of Fig. 8). At bright absolute magnitudes ($-20.5 > M_{1500} < -21.5$) their model LF curve (pink) lies significantly above our measurements. In parameter terms, this discrepancy corresponds to the fainter best-fit characteristic magnitude we obtain in this redshift range ($M^* = -19.12^{+0.20}_{-0.22}$) compared to that found by Arnouts et al. (2005) ($M^* = -19.84 \pm 0.40$). In the other redshift bin (i.e. $0.8 < z < 1.2$), the best fit model curve from Arnouts et al. (2005) lies close to our LF measurements, and our measurement of M^* agrees with that obtained by Arnouts et al. (2005) within 1σ. On comparison of the M^* with Hagen et al. (2015), we find that our values are fainter by at least 3σ in both redshift bins. Their model LF curve (blue) in the lower redshift bin is above our measurements throughout the magnitude range considered in this study. The differences in

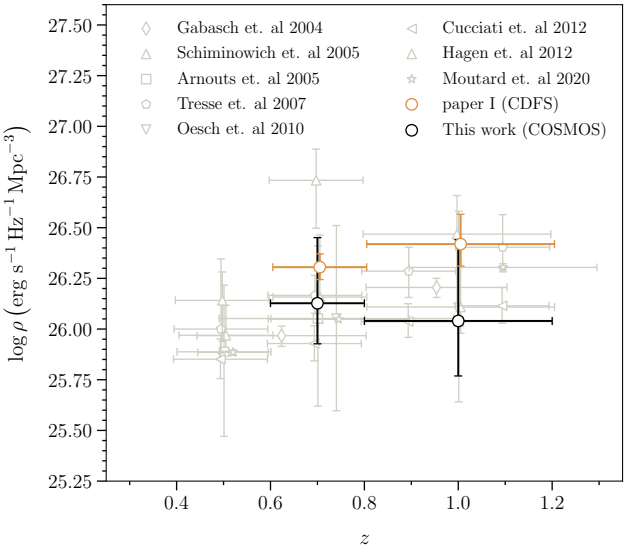

Figure 13. The luminosity density calculated using equation 13. The gray data points are the observed luminosity densities from different past studies. Our estimates for present work (COSMOS) are shown in black colour and those for paper I (CDFS) in yellow. The vertical error bars represent the 1σ (68.26 per cent) uncertainties. The horizontal ones are redshift bin sizes. The data points at same redshifts are slightly shifted for clarity.

Table 6. Luminosity density as a function of redshift. Errors indicate 1σ uncertainties, which include 1σ relative error from cosmic variance.

z	$\rho/10^{26}$ (erg s^{-1}Hz^{-1}Mpc^{-3})	
	This work	paper I[a]
$0.6-0.8$	$1.34^{+1.48}_{-0.49}$	$2.02^{+0.33}_{-0.27}$
$0.8-1.2$	$1.10^{+1.66}_{-0.51}$	$2.62^{+1.06}_{-0.58}$

[a]The error bars in Table 5 of paper I do not include the cosmic variance.

the higher redshift bin become more severe as the absolute magnitude brightens.

Comparing to other recent works, we find our results for α to be in agreement with Page et al. (2021). The work from Oesch et al. (2010) (for $z = 0.75$), who have used the deepest data to date to calculate the LF, obtain parameters which are in good agreement with our results. Their result for α and the break magnitude M^* agrees with our values with deviations well within 1σ.

The two important studies calculating the galaxy LF in the redshift range $0.6-1.2$ using ground based instruments are Cucciati et al. (2012) and Moutard et al. (2020). They derived their estimates by extrapolating their observations taken at longer wavelengths to the UV regime using SED templates. For completion we do compare our results to these works and add the data points from these studies to the luminosity density plot, but we note that comparison of these works with the studies dealing with direct UV surveys should be taken with caution. As compared to Cucciati et al. (2012), we find that our estimates of the faint-end slope at redshift 0.7 are 1σ away from theirs. At the higher redshift bin, our value for α is well within 2σ level from their values in redshift bins centered at 0.9 and 1.1. However, we do find a bigger discrepancy, when we look at the characteristic magnitudes. As compared to our estimates at redshift 0.7, their value is fainter by at least 4σ. For their higher redshift bins at 0.9 and 1.1 we see the difference in the M^* values is 4σ and 2σ significant, as compared to our estimate at redshift 1.0. With regards to Moutard et al. (2020) ($z = 0.75$), our values are in excellent agreement.

We do not put much emphasis on the comparison of the values of the normalisation ϕ^* obtained in this work with any of the previous works and/or paper I. These differences in ϕ^* are expected due to cosmic variance (Trenti & Stiavelli 2008; Moster et al. 2010), between different parts of the Universe explored by different studies. Nevertheless, for completion we plot the estimates for ϕ^* in Fig. 12 (top panel) from this work and some other studies. We would like the remind the reader about the additional errors due to cosmic variance (section 4.4) to be considered, while comparing the resulting value to other works at similar redshifts. Among previous works based on direct observation of the 1500 Å radiation only paper I, Page et al. (2021) and Hagen et al. (2015) estimate the uncertainties in their measurements due to cosmic variance, so we compare our results for normalisation only with these studies. Our estimates for ϕ^* are in very good agreement with Hagen et al. (2015) in both redshift bins. With regards to Page et al. (2021), our values agree at 2σ and 1σ at redshifts 0.7 and 1.0. It should be mentioned however, that due to small sample size, the values obtained by them have large statistical errors. As compared to paper I, we notice smaller values of ϕ^* in both redshift bins. These differences which are significant at $\sim 2\sigma$, can be attributed to known galaxy clusters in the CDFS explored in paper I. Due to the larger sky-area of the COSMOS image, here we have managed to get better constraints on both the normalisation and the cosmic variance. We want to remark here that more independent UV surveys can further help with properly constraining the normalisation of the galaxy LF.

Between the two redshift bin we do not observe any evolution of the faint-end slope. This is in line with paper I and other previous works. However, we do see $\sim 2\sigma$ variation in the characteristic magnitude. As we move from redshift 0.7 to 1.0, the M^* brightens by 0.7 mag. This is very close to 0.8 mag evolution seen in paper I and a similar change in M^* is observed by Hagen et al. (2015). This brightening of the characteristic magnitude supports the currently accepted notion of the star formation history of the universe i.e. the star formation rate decreases as we move from redshifts of around 2 to smaller values. As mentioned earlier, differences in the normalisation are expected due to cosmic variance. We note here that not only for comparison with other studies, but for looking at the potential evolution of normalisation with redshift, these errors need to be considered. As mentioned earlier, due to the large area of the COSMOS UVW1 image, the uncertainties in normalisation due to cosmic variance ($5.4 \times 10^{-2}\,Mpc^{-3}$ and $1.4 \times 10^{-2}\,Mpc^{-3}$ for $z = 0.7$ and $z = 1.0$ respectively) are smaller than the statistical uncertainties. Nevertheless, we include these errors due to cosmic variance in quadrature to statistical errors. We see an evolution in normalisation of the UV LF as it goes down with more than 2σ significance as we move from lower to the higher redshift bin.

The luminosity density in the two redshift bins is calcu-

lated as shown in section 4.3. Our values fall within the error margins of previous works (Fig. 13). Due to the large area of the COSMOS UVW1 image, the errors are dominated by statistical uncertainties. The errors on the luminosity density values of the COSMOS field are larger than those from CDFS, and the values of luminosity density in the CDFS are within the 1σ error bars of the COSMOS values for redshift 0.7 and within 2σ for redshift 1.0 respectively.

7 CONCLUSION

We use the wide area COSMOS imaging survey taken through the UVW1 filter on XMM-OM to calculate the UV LF of galaxies in a redshift range $0.6-1.2$. Using a wide area survey we attempt to extend the analysis to brighter magnitudes, which complements paper I where we calculated the UV LF using a deep survey in the CDFS to constrain the faint-end of the LF.

The binned UV galaxy LF is estimated by using the Page & Carrera (2000) method in the two redshift bins $0.6 < z < 0.8$ and $0.8 < z < 1.2$. The COSMOS imaging pushed the rest frame M_{1500} magnitudes upwards of -21.5 for the redshift bin $0.6 < z < 0.8$ and $\simeq -22$ for the redshift bin $0.8 < z < 1.2$, helping us to to put better constraints on the characteristic magnitude M^* value.

We fit the Schechter function to the data using maximum likelihood to estimate the LF parameters (the faint-end slope, characteristic magnitude and the normalisation). We compare the binned LF shape to the Schechter model. The luminosity function seems to be well described by the Schechter function shape. There is no evolution of α between the two redshift bins. This is also expected from previous works that find an almost constant faint-end slope within the redshift range of our interest. For individual redshift bins, α falls within 1σ margins of values obtained in paper I and all other studies in this redshift range using direct UV measurements. For the characteristic magnitude M_*, we see our derived values are 0.5 to 1 mag fainter than some previous studies. Between the redshift bins under consideration, M_* evolves by $\simeq 0.7$ mag with a $\sim 2\sigma$ significance. An evolution of the M_* by $\simeq 0.8$ mag between the redshift bins was also reported in paper I. With regards to the comparison of values at a particular redshift to the previous works (again using direct UV surveys), our estimates fall within 2σ margins.

As expected for the luminosity density we obtain values relatively smaller than those obtained in the CDFS. However, the differences are significant at $< 2\sigma$ at both redshifts. Between the two redshift bins considered here, the change in luminosity density is not significant enough to infer evolution.

We put a special focus on the bright sources in this study. First we test the most luminous sources, found in the brightest magnitude bins of the LF at both redshifts, for AGN contamination. Then we characterise these objects through an SEDs analysis and by examining their morphologies. At least some of these most powerful UV sources in the COSMOS field seems to be mergers at different stages. Their SEDs and their integrated IR luminosities suggest that these galaxies belong to the (U)LIRG classes, but not the most powerful ones. We think it is mainly because we have removed the bright AGNs from this analysis or because the most luminous galaxies are more heavily obscured than our UV-selected galaxies.

8 ACKNOWLEDGEMENTS

This research makes use of the observations taken with XMM-Newton telescope, an ESA science mission with instruments and contributions directly funded by ESA Member States and NASA. MJP acknowledges support from the UK Science and Technology Facility Council (STFC) grant number ST/S000216/1. MS would like to extend their gratitude towards Vladimir Yershov and Eduardo Ojero for their outstanding support with the XMM-OM software. MS would like to thank Michele Trenti for sharing the source code for their cosmic variance calculator.

9 DATA AVAILABILITY

The data used in this article can be obtained from the *XMM-Newton* Science archive (XSA) at `https://www.cosmos.esa.int/web/xmm-newton/xsa`. We provide the source list used in this paper as a supplementary table with the online version of the paper. Other supporting material related to this article is available on a reasonable request to the corresponding author.

APPENDIX A: CROSS-CORRELATING THE CATALOGUES

Here we calculate the appropriate matching radius for cross-matching our source-list with the ancillary catalogues.

A1 Modeling the source-distribution

The UVW1 source-list is matched to the Laigle et al. (2016) catalogue with a matching radius of 10 arcsec. We plot the distribution of the offsets in Fig. A1. The yellow and blue histograms represent the 'all' and 'best' matches between the Laigle et al. (2016) catalogue and our source-list, as a function of matching radius. Following paper I, we fit a distribution of the form

$$D(x) = A\,\frac{x}{\sigma^2}\exp\left(-\frac{x^2}{2\sigma^2}\right) + m\,x, \tag{A1}$$

to the distribution of all matches, keeping A, σ, and m as free parameters. The first part of equation A1 represents the Rayleigh distribution predicted for the true shape of the actual counterparts (Page et al. 2012) and the second part showing a straight line for the distribution of the spurious counterparts, growing linearly with the matching radius. The fit results are 5251 ± 121 sources, 0.308 ± 0.005 arcsec and 994 ± 21 sources per square arcsec for A, σ, and m respectively. Fig. A1 shows the two elements of the fit, the linear distribution with a slope $m = 994$ sources per square arcsec in green broken and the Rayleigh distribution with amplitude $A = 5251$ and width $\sigma = 0.308$ in broken red curves respectively. The black solid curve shows the total model distribution for all matches.

The distributions in Fig. A1 can used to get an estimate

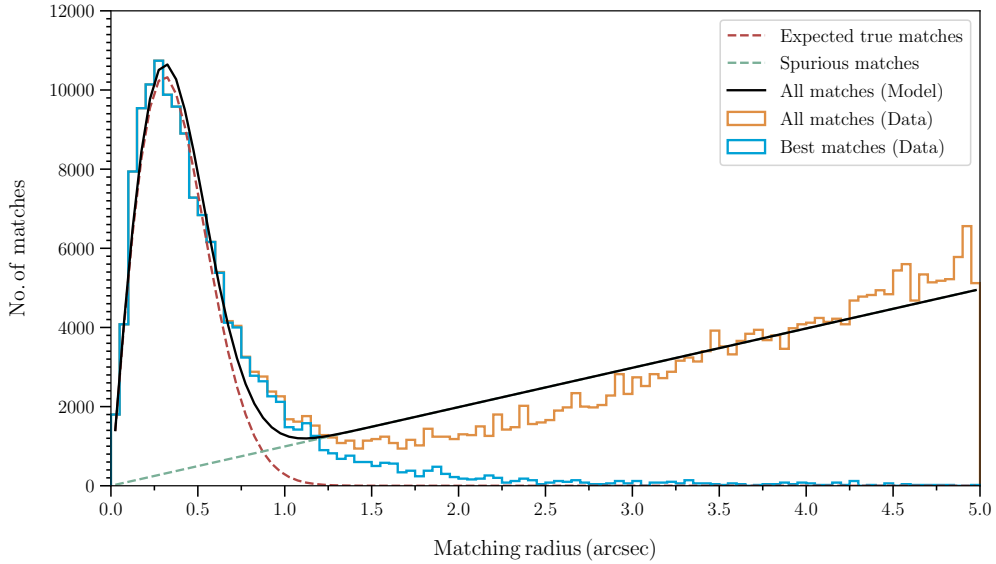

Figure A1. The angular offset distribution histograms are plotted here. The black solid and dashed histograms represent the angular separations corresponding to all and best (closest) matches between the UVW1 source-list and Laigle et al. (2016) catalogue, within a given matching radius. The black solid line shows the expected composite model (Rayleigh + linear) of all matches fitted to the distribution of all matches. The 2σ uncertainty in the fit shown as gray shaded area around it. The components of the composite model i.e. the Rayleigh and the linear models, representing the true and spurious matches, are plotted in dashed orange and blue colours respectively.

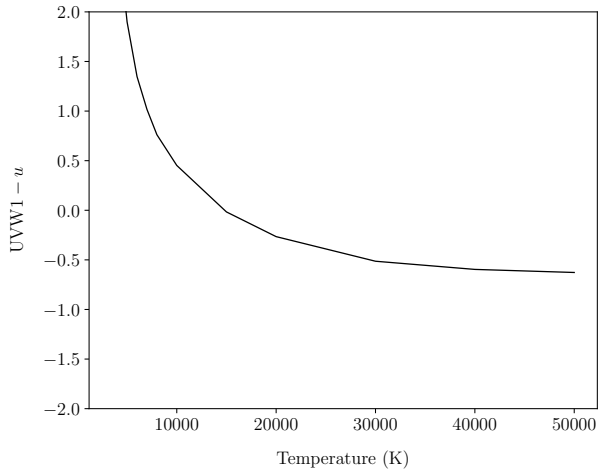

Figure A2. UVW1−u colour as a function of photospheric temperature of the stars.

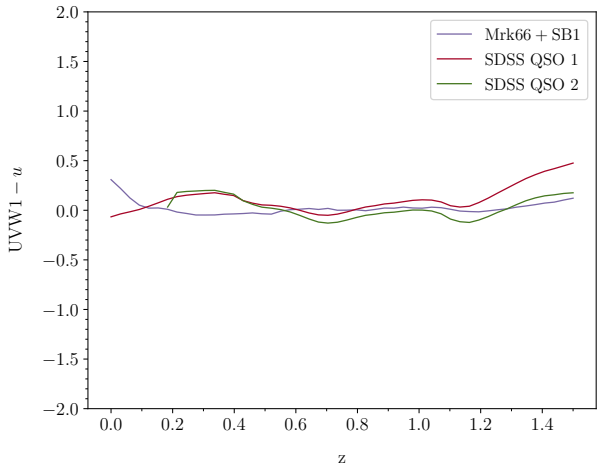

Figure A3. UVW1−u colour tracks for the extended starburst and the two SDSS average quasar templates as function of redshifts.

of the optimum angular radius in order to have minimum number of spurious matches. We can see from Fig. A1, the modelled distribution of true matches (red curve) drops to very small values after 1 arcsec matching radius while the number of spurious matches keeps increasing. So 1 arcsec seems to be a good compromise to have enough matches to build the LF while keeping the spurious sources low. To check this we can see how many sources will get spuriously matched to our UVW1 sources within 1 arcsec. One way to obtain the number of spuriously matched sources is to count the number of sources under the linear distribution in Fig. A1 up to a given matching radius. A total of 497 (9 per cent) and 1118 (17.5 percent) sources are found to be spurious for matching radii of 1 and 1.5 arcsec. These numbers however are upper limits, especially for smaller offset radii, where the linear distribution also has contribution from the distribution of actual matches (i.e. Rayleigh). In the following section we describe further measures that have been used to put additional constraints on the colours of the sources in order to have a reliable source-list while extending the cross-matching radius to 1.5 arcseconds.

A2 UVW1-u colour-cut

In order to avoid missing out on genuine counterparts we need to increase the matching radius while making sure that

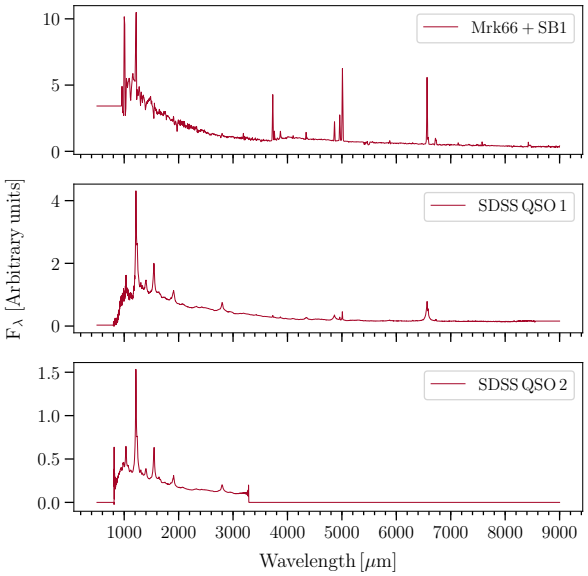

Figure A4. The spectral templates used to calculate the UVW1−u colours of the extended starburst galaxy and the two average SDSS quasar templates.

there are not a lot of spurious matches. To achieve this, we put additional constraints on the colours of the sources. We examine how blue a source can physically be by calculating the UVW1−u colours for stars, quasars and galaxies. We obtain the u colours, we use the CFHT u-band filter.

For stars we use the synthesized stellar spectra from the ATLAS9 project (Castelli & Kurucz 2003) created using the stellar abundances from Grevesse & Sauval (1998). We calculate the UVW1−u colours for these spectra and plot these as a function of their photospheric temperatures in Fig. A2. The UVW1−u colours become more and more blue as the temperature rises and stay close to a value of -0.5 as we approach the hottest photospheric temperatures.

We calculate the colours for quasars from the average SDSS spectral templates from Vanden Berk et al. (2001) and Harris et al. (2016). For the case of galaxies we use the starburst galaxy template (SB1) from Kinney et al. (1996). This template is extended beyond 1250 Å using the spectrum of Mrk 66 from González Delgado et al. (1998). The UVW1−u colours tracks for these galaxies are plotted in Fig. A3. We show the model spectra for the extended starburst and the quasar templates (labelled SDSS QSO 1 and SDSS QSO 2 for Vanden Berk et al. (2001) and Harris et al. (2016) respectively) in Fig. A4.

From the analysis so far we see that the UVW1−u colours can not be theoretically bluer than −0.5. We note that we do not consider effects of reddening for the above calculations, so we keep apply a rather conservative colour-cut of UVW1−u > −1 to our COSMOS UVW1 source-list. Fig. A5 shows the distribution of UVW1−u colours of the UVW1 sources as a function of offset radius for matching with COSMOS 2015 catalogue.

To test the effect of the colour cut we plot distribution of the COSMOS 2015 counterparts of our UVW1 sources before and after the colour cut as a function of matching radius in Fig. A6. The distribution of all matches after the colour

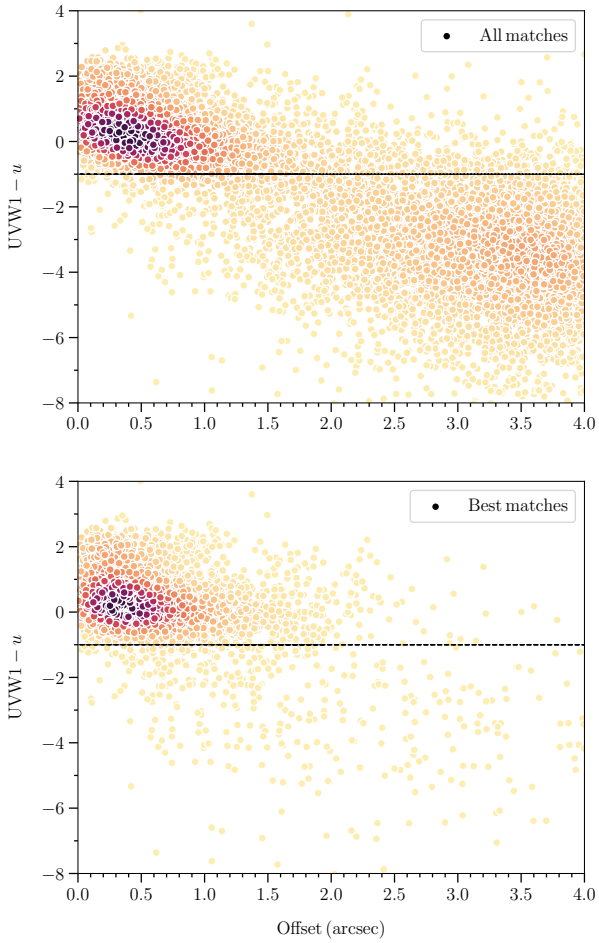

Figure A5. the UVW1−u colours of the COSMOS UVW1 sources as a function of the matching offset for matches with the COSMOS 2015 catalogue. The density of the sources increases from lighter to darker shades. The top and bottom panels separately show the distributions for all and best (closest) matches with COSMOS 2015 catalogue. The black dashed line at UVW1−u = 1 shows the colour cut applied to our source-list.

cut (red solid histogram) approaches the distribution of best matches (red and black dashed histograms). This behaviour follows up to 2.0 arcsec. So, we can use this matching radius for cross matching out UVW1 source-list with other ancillary catalogues provided we apply the colour cut UVW1−u > −1. However, jsut to be on the safe side we use a conservative value of 1.5 arcsec as the matching radius for out cross matching.

REFERENCES

Alam S., et al., 2015, ApJS, 219, 12
Alarcon A., et al., 2021, MNRAS, 501, 6103
Arnouts S., et al., 2005, ApJ, 619, L43
Assef R. J., et al., 2013, ApJ, 772, 26
Behroozi P. S., Conroy C., Wechsler R. H., 2010, ApJ, 717, 379
Bruzual G., Charlot S., 2003, MNRAS, 344, 1000
Bullock J. S., Boylan-Kolchin M., 2017, ARA&A, 55, 343
Calzetti D., Armus L., Bohlin R. C., Kinney A. L., Koornneef J., Storchi-Bergmann T., 2000, ApJ, 533, 682
Cappelluti N., et al., 2007, ApJS, 172, 341

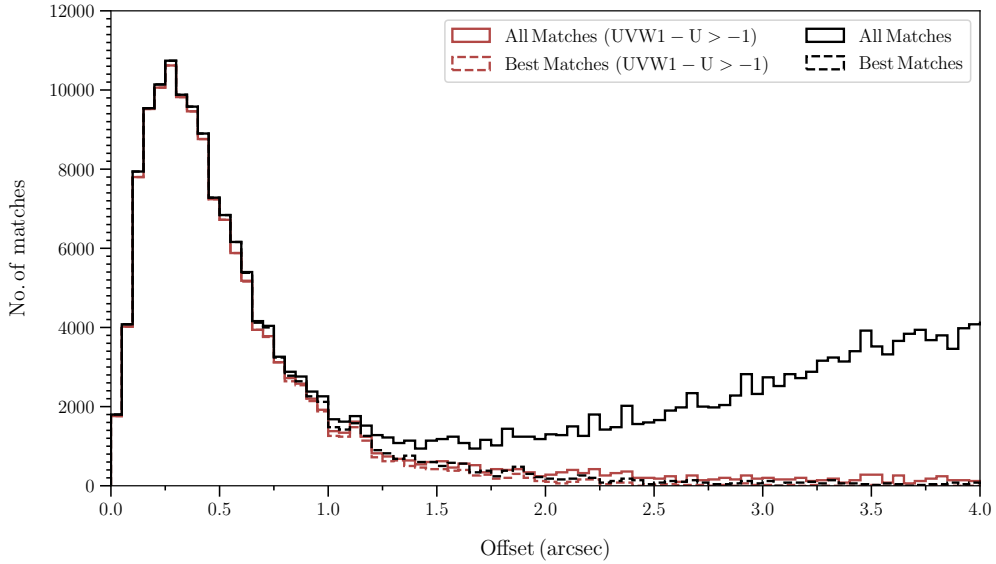

Figure A6. The distribution of matches from COSMOS 2015 catalogue for our UVW1 sources as a function of offset radius. The solid black histogram represents all matches within a given matching radius. The dashed black histogram represents the best matches. The solid and dashed red histograms show distributions of all and best matches after applying the colour cut UVW1$-u > -1$.

Castelli F., Kurucz R. L., 2003, in Modelling of Stellar Atmospheres. (arXiv:astro-ph/0405087)
Chabrier G., 2003, PASP, 115, 763
Coil A. L., et al., 2011, ApJ, 741, 8
Cole S., et al., 2001, MNRAS, 326, 255
Cucciati et al., 2012, A&A, 539, A31
Damjanov I., Zahid H. J., Geller M. J., Fabricant D. G., Hwang H. S., 2018, ApJS, 234, 21
Darvish B., Mobasher B., Martin D. C., Sobral D., Scoville N., Stroe A., Hemmati S., Kartaltepe J., 2017, ApJ, 837, 16
Davies L. J. M., et al., 2015, MNRAS, 447, 1014
Draine B. T., Li A., 2007, ApJ, 657, 810
Fazio G. G., et al., 2004, ApJS, 154, 10
Foreman-Mackey D., Hogg D. W., Lang D., Goodman J., 2013, PASP, 125, 306
Gaia Collaboration et al., 2018, A&A, 616, A1
Gehrels N., 1986, ApJ, 303, 336
Genzel R., et al., 1998, ApJ, 498, 579
González Delgado R. M., Leitherer C., Heckman T., Lowenthal J. D., Ferguson H. C., Robert C., 1998, ApJ, 495, 698
Goto T., et al., 2011, MNRAS, 414, 1903
Grevesse N., Sauval A. J., 1998, Space Sci. Rev., 85, 161
Hagen L. M. Z., Hoversten E. A., Gronwall C., Wolf C., Siegel M. H., Page M., Hagen A., 2015, ApJ, 808, 178
Harris D. W., et al., 2016, AJ, 151, 155
Hasinger G., et al., 2007, ApJS, 172, 29
Hasinger G., et al., 2018, ApJ, 858, 77
Hathi N. P., et al., 2010, ApJ, 720, 1708
Hildebrandt H., Pielorz J., Erben T., van Waerbeke L., Simon P., Capak P., 2009a, A&A, 498, 725
Hildebrandt H., van Waerbeke L., Erben T., 2009b, A&A, 507, 683
Hogg D. W., 1999, arXiv e-prints, pp astro–ph/9905116
Hogg D. W., Baldry I. K., Blanton M. R., Eisenstein D. J., 2002, arXiv e-prints, pp astro–ph/0210394
İkiz T., Peletier R. F., Barthel P. D., Yeşilyaprak C., 2020, A&A, 640, A68
Ilbert O., et al., 2009, ApJ, 690, 1236
Jin S., et al., 2018, ApJ, 864, 56
Kartaltepe J. S., et al., 2010, ApJ, 709, 572
Kashino D., et al., 2019, ApJS, 241, 10
Kennicutt R. C., Evans N. J., 2012, ARA&A, 50, 531
Kinney A. L., Calzetti D., Bohlin R. C., McQuade K., Storchi-Bergmann T., Schmitt H. R., 1996, ApJ, 467, 38
Knobel C., et al., 2012, ApJ, 753, 121
Koekemoer A. M., et al., 2007, ApJS, 172, 196
Laigle C., et al., 2016, ApJS, 224, 24
Leauthaud A., et al., 2007, ApJS, 172, 219
Lilly S. J., Le Fevre O., Hammer F., Crampton D., 1996, ApJ, 460, L1
Lilly S. J., et al., 2007, ApJS, 172, 70
Limber D. N., 1953, ApJ, 117, 134
Madau P., Dickinson M., 2014, ARA&A, 52, 415
Madau P., Pozzetti L., Dickinson M., 1998, ApJ, 498, 106
Marchesi S., et al., 2016, ApJ, 817, 34
Martin D. C., et al., 2005, ApJ, 619, L1
Mason K. O., et al., 2001, A&A, 365, L36
Moster B. P., Somerville R. S., Maulbetsch C., van den Bosch F. C., Macciò A. V., Naab T., Oser L., 2010, ApJ, 710, 903
Moutard T., Sawicki M., Arnouts S., Golob A., Coupon J., Ilbert O., Yang X., Gwyn S., 2020, MNRAS, 494, 1894
Muzzin A., et al., 2013, The Astrophysical Journal Supplement Series, 206, 8
Narayan R., Wallington S., 1993, in Surdej J., Fraipont-Caro D., Gosset E., Refsdal S., Remy M., eds, Liege International Astrophysical Colloquia Vol. 31, Liege International Astrophysical Colloquia. p. 217
Nayyeri H., et al., 2017, ApJS, 228, 7
Oesch P. A., et al., 2010, ApJ, 725, L150
Oke J. B., Gunn J. E., 1983, ApJ, 266, 713
Oliver S. J., et al., 2012, MNRAS, 424, 1614
Page M. J., Carrera F. J., 2000, MNRAS, 311, 433
Page M. J., et al., 2012, MNRAS, 426, 903
Page M. J., et al., 2021, MNRAS, 506, 473
Parsa S., Dunlop J. S., McLure R. J., Mortlock A., 2016, MNRAS, 456, 3194
Paulino-Afonso, Ana Sobral, David Darvish, Behnam Ribeiro, Bruno Smail, Ian Best, Philip Stroe, Andra Cairns, Joseph 2020, A&A, 633, A70
Prescott M. K. M., Impey C. D., Cool R. J., Scoville N. Z., 2006,

ApJ, 644, 100
Sabti N., Muñoz J. B., Blas D., 2021, J. Cosmology Astropart. Phys., 2021, 010
Sanders D. B., Mirabel I. F., 1996, ARA&A, 34, 749
Schechter P., 1976, ApJ, 203, 297
Schlafly E. F., Finkbeiner D. P., 2011, ApJ, 737, 103
Schlegel D. J., Finkbeiner D. P., Davis M., 1998, ApJ, 500, 525
Scoville N., et al., 2007, ApJS, 172, 1
Scranton R., et al., 2005, The Astrophysical Journal, 633, 589
Sharma M., Page M. J., Breeveld A. A., 2022, MNRAS, 511, 4882
Sheth R. K., Tormen G., 1999, MNRAS, 308, 119
Shirasaki M., Ishiyama T., Ando S., 2021, ApJ, 922, 89
Somerville R. S., Davé R., 2015, ARA&A, 53, 51
Somerville R. S., Lee K., Ferguson H. C., Gardner J. P., Moustakas L. A., Giavalisco M., 2004, ApJ, 600, L171
Stern D., et al., 2012, ApJ, 753, 30
Symeonidis M., Page M. J., 2021, MNRAS, 503, 3992
Trenti M., Stiavelli M., 2008, ApJ, 676, 767
Trump J. R., et al., 2009, ApJ, 696, 1195
Vanden Berk D. E., et al., 2001, AJ, 122, 549
Wright E. L., et al., 2010, AJ, 140, 1868
Yang X., Mo H. J., van den Bosch F. C., 2003, MNRAS, 339, 1057
Yoshida M., et al., 2006, ApJ, 653, 988
Yoshiura S., Oguri M., Takahashi K., Takahashi T., 2020, Phys. Rev. D, 102, 083515
van der Wel A., et al., 2016, ApJS, 223, 29

This paper has been typeset from a TEX/LATEX file prepared by the author.